Université d'Ottawa · University of Ottawa

Semiconductor Quantum Dot Lasers

by
Karin Hinzer

Thesis submitted to the Faculty of Graduate Studies and Research
in partial fulfillment of the requirements for the degree of
Master of Science in Physics

Department of Physics
University of Ottawa
Ottawa-Carleton Institute for Physics
Ottawa, Canada
1998

0-612-36702-9

Abstract

Stimulated emission in semiconductor quantum dot (QD) laser structures is demonstrated. Red-emitting, self-assembled QDs of highly strained InAlAs were grown by molecular beam epitaxy on GaAs substrates. Carriers injected electrically from the doped regions of separate confinement heterostructures thermalized efficiently into the zero-dimensional QD states, and stimulated emission at ~ 707 nm is observed at 77 Kelvin with a threshold current of 175 milliamperes for a 60-μm by 400-μm broad area laser. A measured external quantum efficiency of ~8.5 % at low temperature with a peak power greater than 200 milliwatts demonstrate good size distribution and high gain in these high-quality QDs.

Results from structures with contact layers designed to improve carrier confinement, show a lower threshold current density at low temperatures, and are able to operate up to room temperature. At low temperatures (4-50 K), stimulated emission occurs via excited state of the QDs, followed by a gradual stimulated transition from the excited states to the ground state for temperatures ranging from 50 K to 140 K. Above 140 K, lasing occurs at the ground states transition of the QDs up to room temperature.

At low temperatures, the lasing threshold currents are found to be more temperature insensitive than for two-dimensional quantum well (QW) lasers. At higher temperatures, the threshold current are governed mainly by the depth of the separate confinement region. For samples with multiple QD layers displaying vertical self-assembling, a broadening of the stimulated emission energy linewidth is observed.

À Bruno

Statement of Originality

Except where otherwise stated, the results presented in this thesis were obtained by the author during the period of her M.Sc. research project under the supervision of Dr S. Charbonneau and in strong collaboration with Dr S. Fafard. They are to the best of her knowledge original. These include:

1. Electroluminescence study of InAlAs/AlGaAs QD lasers as a function of injection current and temperature.
2. Photovoltage and photoluminescence study of InAlAs/AlGaAs QD laser structures at $T = 77$ and 300 K.
3. Threshold current density and current-voltage characterization of InAlAs/AlGaAs QD lasers.
4. Laser structure waveguide analysis and confinement factor numerical calculations including figure 2.8.

The TEM micrograph of figure 3.3a was produced by J. McCaffrey and figures 3.3b and 3.3c were provided by Dr. E.M. Griswold. The electroluminescence spectra of figure 4.2 were acquired by S. Raymond and the spectra in figure 4.12 were obtained in collaboration with J. Arlett. Samples *Ia-c* and *III* were grown at the Institute for Microstructural Sciences, National Research Council by Dr. S. Fafard and samples *IIa-b* were designed at NRC but were grown at Nortel Technologies by Dr. A.J. SpringThorpe. Samples were laser processed by Dr. Y. Feng.

- <u>The above work has led to the following papers:</u>

S. Fafard, **K. Hinzer**, S. Raymond, M. Dion, J. McCaffrey, Y. Feng, and S. Charbonneau, Red-emitting semiconductor quantum dot lasers, Science. **274**, 1350 (1996).

S. Fafard, **K. Hinzer**, A.J. SpringThorpe, Y. Feng, J. McCaffrey, S. Charbonneau, Temperature effects in semiconductor quantum dot lasers, Mat. Sci. & Eng. B **51**, 114 (1998).

K. Hinzer, S. Fafard, A.J. SpringThorpe, J. Arlett, E.M. Griswold, Y. Feng, Room temperature operation of AlInAs/AlGaAs quantum dot lasers, Physica E **2**, 729 (1998).

F. Yang, G.C. Aers, **K. Hinzer**, Y. Feng, S. Fafard, S. Charbonneau, E.M. Griswold, A.J. SpringThorpe, Visible quantum dots under reverse bias, *submitted to SPIE Proc. June 1998.*

- <u>Portions of the results in this thesis were presented in the following conferences:</u>

K. Hinzer, S. Fafard, J. McCaffrey, S. Raymond, Y. Feng, M. Dion, S. Charbonneau (August 1997) Optical properties of InAlAs quantum dot lasers, oral presentation at the *Eighth Canadian semiconductor technology conference*, Ottawa, Canada.

K. Hinzer, S. Fafard, J. McCaffrey, S. Raymond, Y. Feng, M. Dion, S. Charbonneau (July 1997) Stimulated emission in red-emitting semiconductor quantum dot heterostructures, poster at the *Eighth international conference on modulated semiconductor structures*, Santa-Barbara, United-States.

K. Hinzer, Optical properties of InAlAs quantum dot lasers, presented as a talk at the 1997 Fall OCIP graduate students seminar at Carleton University

- <u>Contributions not directly related to this thesis:</u>

J. Arlett, F. Yang, **K. Hinzer**, S. Fafard, Y. Feng, S. Charbonneau, R. Leon, Temperature independent lifetime in InAlAs quantum dots, J. Vac. Sci. Technol. B **16**, 578 (1998).

Acknowledgements

I would like to thank my dynamic and supportive supervisor Sylvain Charbonneau for allowing me to work in a laboratory with state-of-the-art equipment, for his guidance all along the project, and for his unfailing enthusiasm. I would like to thank Simon Fafard for the chance to work on such an interesting project, the tremendous help in the lab, the many discussions and also for designing and growing the samples.

I am indebted to Sylvain Raymond for previous characterization done on this quantum dot system and to Jessica Arlett, NRC-summer student, for assistance in measurements over the summer. I have received ongoing support from Yan Feng, Michel Dion and the entire IMS-Microfabrication group in laser processing, and TEM micrographs essential for sample characterization from John McCaffrey. I am also grateful to André Delage for his help on performing waveguide analysis.

During the long period the IMS MBE was offline, I benefited from Tony SpringThorpe's sample growth and Ellen Griswold's TEM micrographs, who are both from Nortel.

Finally, I would like to thank Bruno for his immense support and both of our families for their encouragement over the last two years.

Table of Contents

List of Figures

List of Tables

List of Abbreviations

DOS	Density of states
EL	Electroluminescence
FWHM	Full width at half maximum
I_{exc}	Excitation intensity
J_{th}	Threshold current density
MBE	Molecular beam epitaxy
ML	Monolayer
PL	Photoluminescence
PV	Photovoltage
QD	Quantum dot
QW	Quantum well
SIMS	Secondary ion mass spectroscopy
TEM	Transmission electron microscopy
WL	Wetting layer

Chapter 1

INTRODUCTION

The introduction of heterostructures in 1970 [1] marked the beginning of quantum confinement in semiconductor lasers. The simplest example of a heterostructure is obtained when layers of semiconductors with larger bandgap energies surround a lower bandgap material. Either one of these layers can be doped with donor or acceptor impurities, with the possibility of forming a *p-n* junction at one of the hetero-interfaces. Basic understanding of such low-dimensional systems and applicability of heterostructure concepts has become possible in recent years due to improvement of growth techniques such as molecular beam epitaxy (MBE).

The energy band in a semiconductor crystal results from the periodic structure of an infinite lattice. When the crystal thickness is finite and thin enough to be comparable with the de Broglie wavelength of an electron in a semiconductor ($\approx$ 10 nm), one obtains a structure confined in one-dimension known as a quantum well (QW). Perpendicular to the well plane (z-direction), electrons are confined by the potential well created by the double heterostructure, resulting in a structure having discrete quantized energy levels. Along the well plane (x-y plane), the crystal is assumed infinite. The density of states of carriers in the QW is modified from the conventional $E^{1/2}$-dependence for bulk materials to a step-like dependence [2]. Such lower dimensional structures can be used as the active region of semiconductor lasers. It was first predicted theoretically, and subsequently confirmed experimentally, that this reduction in dimensionality of the active region results in superior lasing characteristics including lower threshold currents and improved temperature stability. Today, semiconductor laser diodes based on QWs are the key components in optoelectronic and photonic integrated circuits, and play an essential role in the expanding information technology and communication industry [3]. They are used in a wide range of applications from optical fiber communication systems to barcode scanning, including optical storage, image recording, and displays for entertainment and instrumentation. These devices are capable of high powers and efficiencies at a variety of wavelengths in the visible and the infrared.

By increasing the confinement of carriers in the other directions (x and y), systems with lower dimensions can be obtained: quantum wires (QWRs) and quantum dots (QDs), in which carrier motion is confined to one and zero dimension respectively. Because of the 3D-quantum confinement, the energy spectra of electrons and holes in QDs can be considered discrete. This delta-function-like density of states of QD systems leads to an effective absence of carrier thermal distribution, independent of temperature, in contrast to QW and bulk structures. The main expected advantage in introducing QDs as the active medium of a semiconductor laser over conventional QW lasers is a lowering in threshold current density due to the discrete nature of the density of states [4]. Other predicted advantages include: higher modulation speed, reduced temperature sensitivity, higher optical gain, and wider spectral gain profiles [4-7]. For these reasons, structures with QDs as active regions have generated much interest recently as a new class of artificially structured materials having discrete atomic-like states with tunable energies, through composition and size variations, that are ideal for use in laser structures.

Prior to 1994, only one research group had reported light emission from quantum dots through current injection [8], using standard lithographic techniques for the fabrication of QDs. An important advance in the fabrication of zero dimensional structures exploits one of the natural consequences in growth modes for dissimilar materials. QDs grown in this manner make use of a mature epitaxy growth process without requiring any additional processing. As well, their ability to emit at a range of wavelengths by simply using the various well understood and characterized III-V alloy systems, make them perfect for immediate integration into practical devices. The samples characterized in this study were grown using this fabrication technique.

This thesis focuses on the optical properties of self-assembled quantum dots grown in the InAlAs/AlGaAs alloy system, and more specifically on their use as active material in QD lasers. QDs made of this material system have emission wavelengths corresponding to the red (650-730 nm) portion of the spectrum [9] allowing for possible applications in higher-density optical storage, or in display and illumination. Chapter 2 begins with a review of the basic properties of QDs and goes on to describe gain and waveguide analysis in heterostructure lasers. Chapter 3 includes a description of the samples, laser fabrication, optical measurement techniques, and apparatus. Results obtained from measurements of $In_{0.64}Al_{0.36}As$/AlGaAs QD lasers are presented and discussed in chapter 4, beginning with the evidence for stimulated emission from QDs. The effect of potential barrier height of the confining layers on laser characteristics is analyzed, and the properties of lasers grown with multiple QD layers are presented.

Finally, a summary of the results and comparison with other systems appears in the conclusion.

Chapter 2

THEORY

This chapter is intended to give background information on the system studied and is divided into three sections; the first describes growth methods and basic optical properties of QDs while the second evaluates the energy levels and density of states for idealized heterostructures followed by the equations used to calculate the energy levels of a more realistic system: the lens shaped quantum dot. The chapter concludes with a discussion of gain and threshold current density in heterostructures of different dimensionality as well as an analysis of light propagation in slab waveguides.

2.1 Growth method and basic optical properties of QDs

Zero-dimensional semiconductor structures may be obtained through epitaxial growth techniques. Two principal methods can be distinguished: (1) the growth of two-dimensional layered structures (QWs) followed by successive etching procedures that lowers the dimension; and (2) epitaxial techniques utilizing self-organized island formation in highly mismatched (~ 4%) epilayer/substrate growth systems.

The first method for nanofabrication of semiconductor materials uses lithographic and etching techniques to produce dots with diameters of ~25 nm [10-14]. Other fabrication techniques used in production of QDs include intermixing where a focussed ion beam having a diameter of 50 nm was used to modify the lateral bandgap profile [15], gate modulation of patterned confining layer [16] and overgrowth on vicinal surfaces [17]. It has been shown that the etching techniques required in the fabrication of QDs through pattern transfer onto semiconductors introduces additional damage forming a depletion layer at the surface of the patterned device, and thus affects the electronic properties of the materials. This damage manifests itself on a microscopic level in the form of nonradiative defects such as dislocations and vacancies [18]. In the case of gate modulation devices and intermixing techniques, reduced carrier confinement are obtained, making the observation of quantum effects possible only at very low temperatures. Dots may also be obtained by growth of nanocrystals in glass matrices, and in organic materials and related matrices [19]. Electrical injection of carriers is difficult in these systems however, making them less than ideal candidates for device applications.

The second class of "nanofabrication" technique, which relies on the formation of lower dimensional structures during epitaxial growth, has recently attracted a lot of interest. Strain induced self-assembled growth leads to the formation of small dots (about 10 - 30 nm diameter) having good size uniformity, and a high density (between 10^8 to 10^{11} dots/cm^2). In the past five years, dots have been grown in a variety of III-V semiconductor systems including InAs/GaAs [20], InAlAs/AlGaAs [9], and InAs/InP [21], in II-IV materials like CdSe/GaAs [22] and in the indirect bandgap group-IV system SiGe/Si [23]. Since the fabrication of dots is intrinsic to the growth method used, this technique is attractive for device applications mostly through its compatibility with commercial growth systems as well as the availability of ultra pure elements needed for growth. Control of the QD energy levels is possible by varying the growth conditions. For example, S.-Z. Chang, T.-C. Chang, and S.-C. Li have observed that for systems with low lattice mismatch (1-2 %), the QD density is high and the QD sizes are small; for larger lattice mismatch (> 2 %), the QD density is lower and the QD sizes are larger [24]. The growth temperature is another important factor in determining both the ground state energy level and the intersublevel spacing of the QDs [25]. The QDs used in this study were obtained through spontaneous island formation.

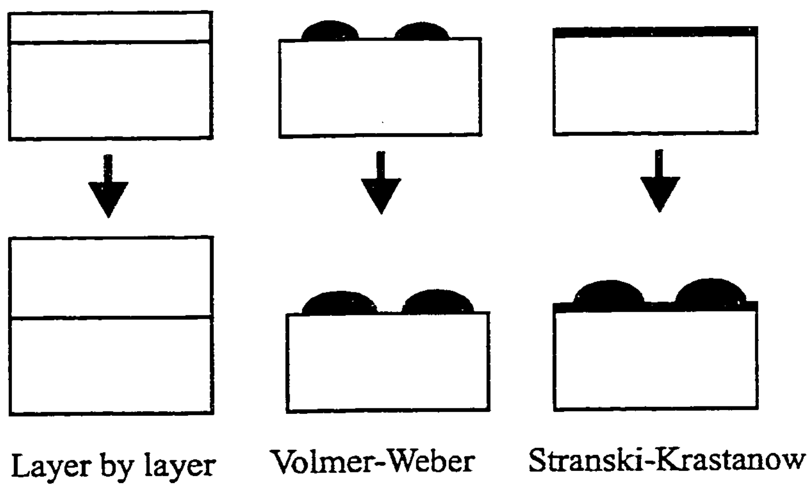

Figure 2.1 Schematic representation of the three possible growth mechanism of thin epitaxial films.

There are three known modes of heteroepitaxial growth [23]: Frank-van der Merve mechanism or layer-by-layer growth [26], Stranski-Krastanow mechanism or layer-by-layer growth followed by 3D island formation [27], and Volmer-Weber mechanism or island growth [28] (figure 2.1). The selection of one growth mode over another depends on the epitaxial layer and the substrate on which it is to be grown. In fact it was shown that, owing to the difference in nature and strength of the chemical bonds, and the lattice parameters, the three growth modes could be covered [29]. Because of these fundamental parameters (bond strength and lattice parameters), the chemical potential of the overgrowth differs from that of an infinitely large crystal. Across the interface, the atoms of the deposit can be bound more loosely (or tightly) to the substrate atoms than to the atoms of the same crystal. Consequently, the chemical potential of the first layers of the deposit could be higher (or lower) than the chemical potential of the infinitely large deposit crystal. The Volmer-Weber growth mode occurs when the interfacial bonding is weaker than the bonding in the deposit itself, that is, the adatoms will have a tendency to form islands on the surface to minimize the interface area. In systems having strong interfacial bonding, layer by layer growth occurs; the atoms "wet" the entire surface. At this point, the lattice misfit plays a prominent role in determining the growth mode. The larger the misfit, the greater the tendency towards island growth, and vice-versa. Generally, layer-by-layer growth occurs if the misfit is small. If the misfit is substantial, coherently strained islands grow on top of the wetting layer (WL) until they reach the dislocation-formation critical thickness. This is known as the Stranski-Krastanow growth mode. The size and shape dispersion of these islands is very small at the onset of island growth. If the growth is allowed to proceed above the critical thickness with the same lattice mismatched material, generation of dislocations at the interface between the layer and the substrate will occur, producing strain relaxation. Once formed, these incoherent, strain-relaxed islands, continue to grow with little restriction until a complete two-dimensional film has been developed. If, on the other hand, before reaching the critical thickness, the dislocation-free dots are capped with a material having the same lattice constant as the substrate, the growth proceeds epitaxially without introduction of dislocations. The QDs are then sandwiched between two similar epilayers.

The optical excitation of self-assembled QD systems yields bright luminescence and generally reveals a Gaussian line shape distribution (figure 2.2a). In the case where nonresonant excitation is used, photoluminescence (PL) data display smooth and structureless spectra. Typically for such PL experiments, the spot size is of the order of 100 μm diameter, and therefore for characteristic dot densities of 200 μm^{-2}, a large number of QDs are probed (~ 10^6 dots). The PL data therefore reflects the statistical distribution of the ground state energy levels of the individual dots that arises from the slightly different zero dimensional confining potentials. Since the QDs have a deep confining potential and a relatively small height-to-diameter ratio, this distribution should arise mainly from the additional atoms along the growth direction. Other parameters, such as small variations in the diameter, in the alloy composition, or in partial (defect-free) strain relaxation, can also contribute to the observed inhomogeneous broadening in the emission spectrum.

A smaller number of QDs can be probed through the use of mesas, etched from the QD structure, of different sizes [9] or simply by performing micro-PL, where the probing laser spot size is reduced to the diffraction limit (~ 1 μm). Figure 2.2b shows the results obtained on mesas of different sizes (3, 7 and 13 μm^2) obtained from the same sample as in figure 2.2a, having a dot density estimated at 200 per μm^2 (from TEM plane view measurements). The corresponding number of dots probed is estimated at N ~ 600, 1400, and 2500 dots respectively. For the small mesas containing only a few hundred dots, the PL spectrum displays distinct, very narrow lines (full with at half maximum (FWHM) ~ 100 μeV). As the number of dots probed increases, the spectra become smooth, as expected, by considering the statistics of large number of added lines. The appearance of the sharp spectral lines is an indication of the zero-dimensional nature of the density of states (DOS). As the temperature of the system is increased, the sharp spectral features observed in the small mesa PL spectra do not broaden [31].

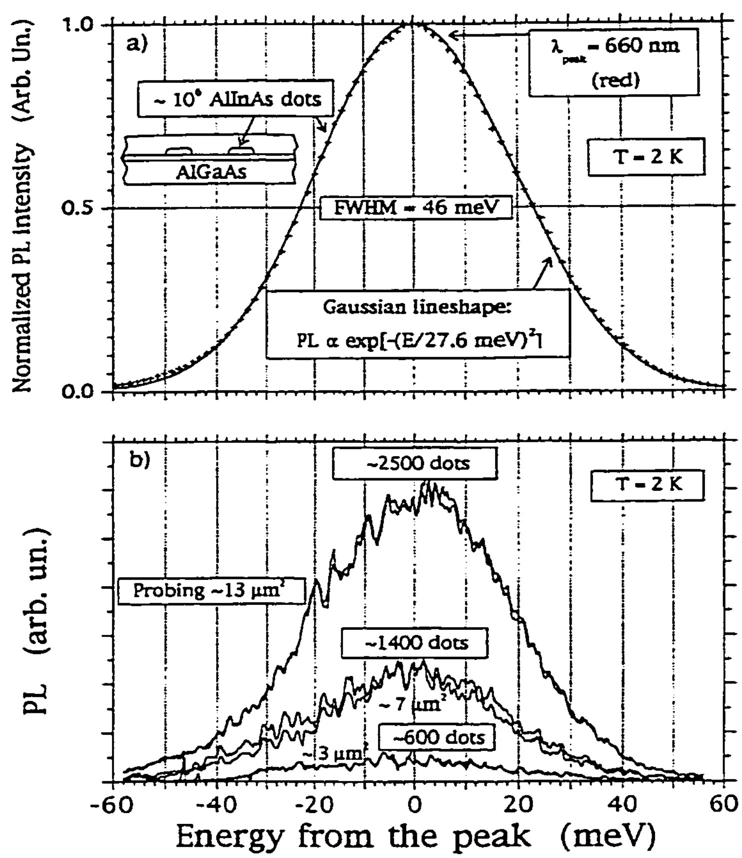

Figure 2.2 (a) Low-temperature PL spectra obtained with an InAlAs/AlGaAs QD sample, probing a large ensemble (~10^6) of 17-nm diameter dots under the excitation spot, and a Gaussian distribution fit. (b) PL of *N*-dot ensembles delineated with μm-size mesas, displaying statistical fluctuations. Two scans are shown for each mesa to evaluate the reproducibility of the sharp features. The peak position for the InAlAs/AlGaAs QD ensembles is $\lambda = 660$ nm [9].

This temperature-independent emission linewidth was predicted theoretically and is simply a consequence of the δ-function like density of states due to the zero-dimensional nature of the dots. Exciton lifetime measurements done on these sharp spectral features were shown to be constant with temperature [31, 32] up to the onset of thermionic emission; a further evidence of the zero-dimensional nature of these self-assembled dots.

The atomic-like discrete energy spectrum of each QD state can easily lead to a state-filling effect at higher optical excitation, due to the exclusion principle when only a few carriers can populate the lower states. In fact, in recent publications it was emphasized that only two electrons can occupy the ground state level of a dot (spin up and spin down), four electrons in the first excited state ($n = 2$) and so on [33]. This causes hindered inter-sublevel dynamics and observation of excited state interband transitions as the excitation intensity is increased. State-filling will show clear saturation effects as well. At low excitation intensities, only the (inhomogeneously broadened) ground state levels are generally observed because of the fast inter-sublevel relaxation process taking place. As the intensity is increased, a progressive saturation of the lower energy transitions is combined with the emergence of new emission peaks originating from the excited state interband radiative transitions. These effects are observed as the inter-sublevel carrier relaxation towards the lower levels is slowed due to the reduced number of available final states [34-36]. An example of state-filling effect, where the intersublevel spacing is larger than the inhomogeneous broadening, is depicted in figure

2.3 for the InGaAs/GaAs system [37]. QDs having larger dimensions or deeper potentials are expected to have more bound states.

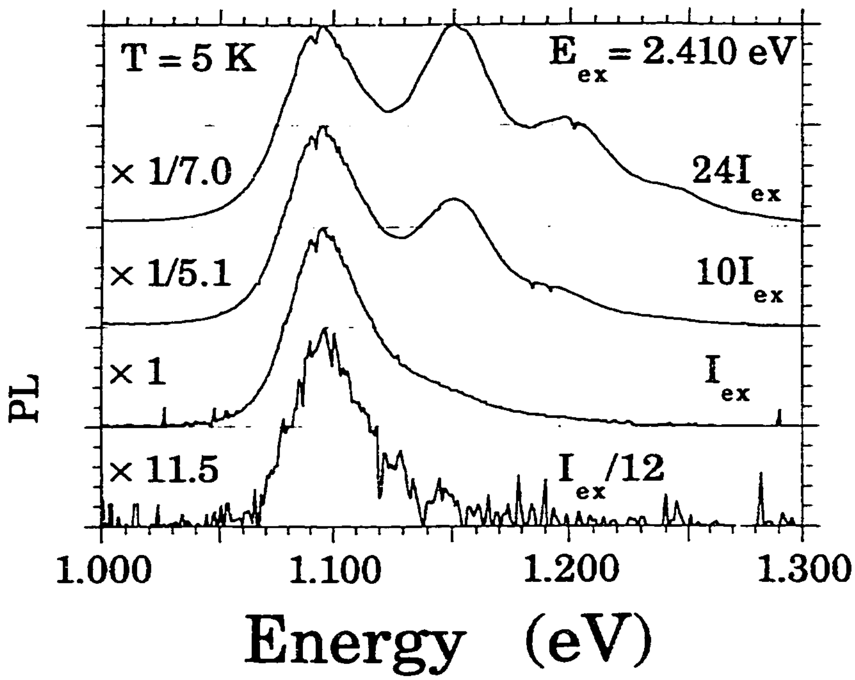

Figure 2.3 PL spectra obtained at T = 5 K with different excitation intensities (I_{ex}) with $In_{0.5}Ga_{0.5}As/GaAs$ QD's, 36.5 nm in diameter, displaying strong level filling and emission from the excited states and saturation of the ground states with increasing excitation intensities. I_{ex} ~ 10 W/cm^2 [37].

2.2 Energy levels and density of states for idealized quantum wells and quantum dots

The advantages of using low-dimensional structures arise mainly from the changes in the density of states as discussed previously [4]. The density of states for electrons and holes in basic systems are calculated using Schrödinger's equation [38, 39]:

$$-\frac{\hbar^2}{2m^*}\nabla^2\Psi + V\Psi = E\Psi \ , \qquad (2\text{-}1)$$

where m^* is the particle effective mass and E represents the energy of the particle from the band edge. The hard wall approximation for the potential is used, i.e. the potential V is zero inside the structure and the barriers are infinite. In the case of a cubic potential, separation of variables is applied to solve equation 2-1. For free-particles, the wavefunctions have the form of a travelling plane wave

$$\Psi_v = e^{ik_v x_v} \quad , \qquad (2\text{-}2)$$

where k_v is the particle wavevector with the allowed values $k_v = \pi n_v / L$ and $n_v = \pm 1, \pm 2, \ldots$ In Cartesian coordinates, v can be replaced by x, y or z and L represents a macroscopic length. In the case of particles confined to a microscopic dimension, the particle energy levels are quantized and the wavefunction becomes

$$\Psi_v = \sqrt{\frac{2}{l}}\sin(k_v x_v) \quad , \qquad (2\text{-}3)$$

where l_v is a microscopic length and $k_v = \pi n_v / l_v$ with $n_v = 1, 2, \ldots$ The total energy is given by:

$$E = \frac{\hbar^2}{2m^*}\left(k_x^2 + k_y^2 + k_z^2\right) \ . \qquad (2\text{-}4)$$

For a two-dimensional quantum well, the motion along the growth direction (z) is quantized, so the allowed energies in the z-direction are

$$E_{n_z} = \frac{\hbar^2}{2m*}\left(\frac{n_z \pi}{l_z}\right)^2 \quad . \tag{2-5}$$

The particle wavefunction Ψ is confined to the well width l_z. The density of states up to and including those of energy E is equal to:

$$\rho^{2D}(E) = \frac{m^*}{\pi \hbar^2 l_z} \sum_{n_z} \theta\left(E - E_{n_z}\right) , \tag{2-6}$$

where $\theta(E)$ is the unit step function [$\theta(E \geq 0) = 1$ and $\theta(E) < 0) = 0$] and n_z is the subband quantum number. Therefore the two-dimensional density of states has a staircase shape, as shown in figure 2.4a.

For quantum dots, quantization occurs in all three directions and the allowed energies are

$$E_{n_x n_y n_z} = \frac{\hbar^2 \pi^2}{2m^*}\left(\frac{n_x^2}{l_x^2} + \frac{n_y^2}{l_y^2} + \frac{n_z^2}{l_z^2}\right) , \tag{2-7}$$

with a zero-dimensional density of states expressed as:

$$\rho^{0D}(E) = \frac{1}{l_x l_y l_z} \sum_{n_x, n_y, n_z} \delta\left(E - E_{n_x n_y n_z}\right) , \tag{2-8}$$

where n_x, n_y, and n_z are the quantum numbers for the allowed energies in the respective directions. This density of states has discrete values as can be observed in figure 2.4b.

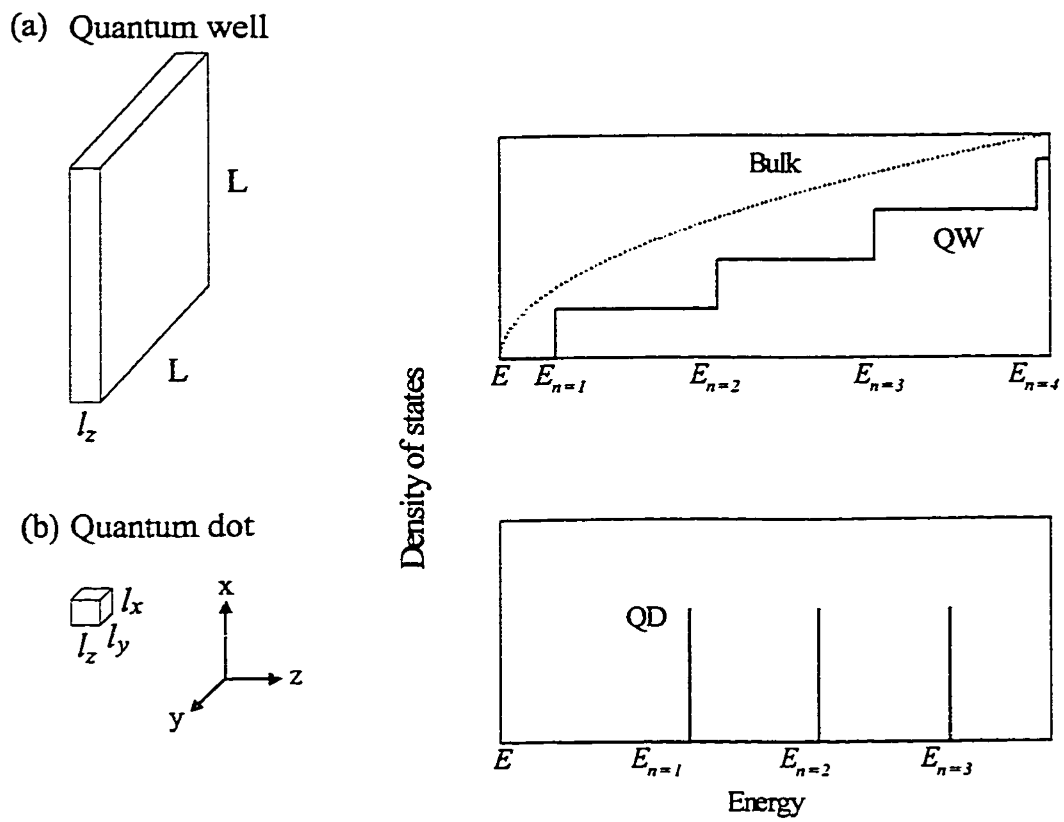

Figure 2.4 Density of states for particles confined in (a) two dimensions (the bulk density of states is shown for comparison), and in (b) zero dimensions.

As the dimensionality of the structure is decreased, the density of states becomes increasingly discontinuous and the onset of energy levels shifts towards higher values. These effects are independent of the shape of the structure studied, as long as comparison is done between structures of macroscopic and microscopic dimensions.

In the case of self-assembled quantum dots, the density of states calculation must take additional factors into account, the most important being the size/composition inhomogeneity of the dot population. The allowed carrier energy level positions and intersublevel spacings in the QDs will then vary slightly for dots of different size/composition. This will result in a state distribution having a certain width: the larger the population inhomogeneity, the wider the distribution.

2.3 Energy levels in a lens shaped quantum dot

In the InAlAs/AlGaAs system, the quantum dots can be modeled as lens-shaped (see figure 3.3). Such modeling has been done previously [33, 40] with numerical results for QDs in the InGaAs/GaAs system. The disks are on top of a narrow quantum well, also known as the wetting layer, of thickness t_w, and can be modeled as part of a sphere of fixed height l_0 and base radius ρ_0 as shown in figure 2.5. The bottom of the conduction band of the WL and QD material is below the bottom of the conduction band of the surrounding material. The carriers, confined to a thin QW, are further localized in the

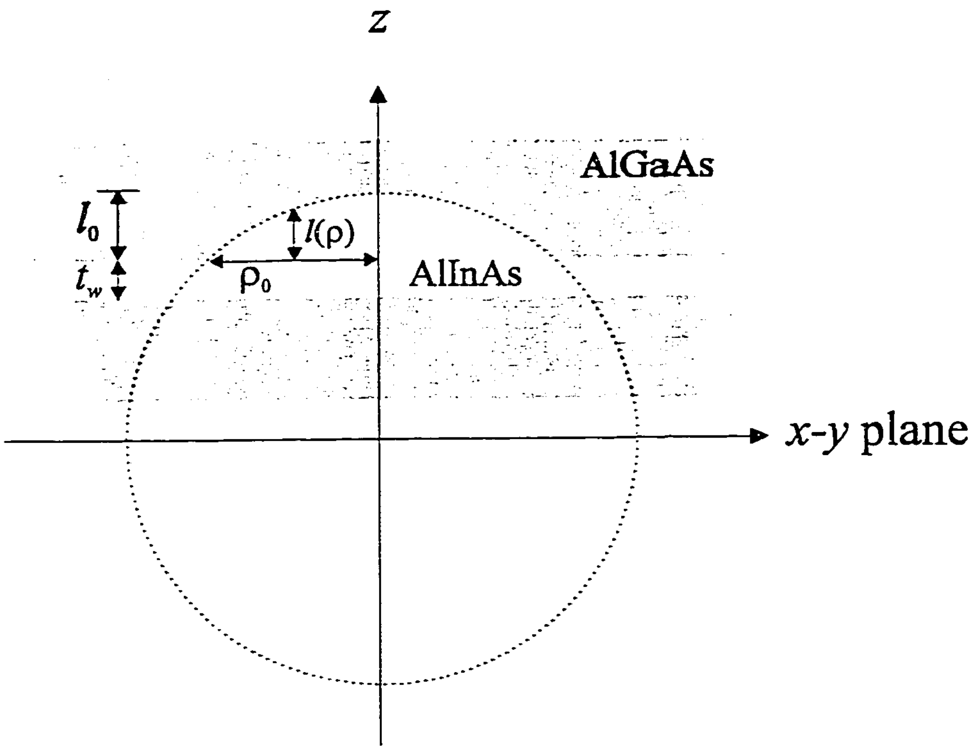

Figure 2.5 Cross section view of an ideal lens-shaped quantum dot.

area of the dot due to the effectively increased thickness of the layer at these points. The dots have a base diameter in the nanometer range, so that lateral confinement is not negligible.

If an electron-hole pair is trapped in a lens-shaped dot, the effective Hamiltonian can be expressed as:

$$H = \frac{P_e^2}{2m_e} + \frac{P_h^2}{2m_h} - \frac{e^2}{\varepsilon |r_e - r_h|} + V(\mathbf{r}_e) + V(\mathbf{r}_h) \ , \quad (2\text{-}9)$$

where the subscripts e and h stand for electron and hole, $V(r_e)$ and $V(r_h)$ are the carrier confining potentials due to the dot shape and the middle term is the Coulomb interaction inside the dot. For dots of small dimensions in the so-called strong confinement range ($R \ll a_B$, where R is the electron-hole distance and a_B is the excitonic Bohr radius), Coulomb interaction effects are neglected [41]. The problem therefore simplifies to the one-particle effective-mass Schrödinger equation (equation 2-1) for both electrons and holes. The adiabatic approximation is used to model the confining potential $V(r)$ for the dot. This method states that the potential a particle feels, when moving in the x-y plane, is given at each point by the ground state energy of a quantum well of equivalent thickness $l(\rho)$. The confining potential is zero inside the dot and wetting layer, but finite outside. Equation 2.1 can be transformed into an equivalent system of equations [33]:

$$-\frac{\hbar^2}{2m_w^*}\frac{\partial^2\Phi_x(x)}{\partial x^2}+V_x^{eff}\Phi_x(x)=E_x\Phi_x(x) \tag{2-10a}$$

$$-\frac{\hbar^2}{2m_w^*}\frac{\partial^2\Phi_y(y)}{\partial y^2}+V_y^{eff}\Phi_y(y)=E_y\Phi_y(y) \tag{2-10b}$$

$$-\frac{\hbar^2}{2m^*(z)}\frac{\partial^2\Phi_z(z)}{\partial z^2}+V_z^{QW}\Phi_z(z)=E_z\Phi_z(z) \tag{2-10c}$$

$$E=E_x+E_y+E_z \quad \text{and} \quad \Psi=\Phi_x\Phi_y\Phi_z\ . \tag{2-10d}$$

V_z^{QW} is the potential of an InAlAs/AlGaAs quantum well of width l_0+t_w, $V_x^{eff}=E^{QW}(l(x))-E^{QW}(l_0+t_w)$ and $V_y^{eff}=E^{QW}(l(y))-E^{QW}(l_0+t_w)$ are the effective potentials obtained from the adiabatic approximation. $m_z^*(z)$ is replaced by the AlInAs effective mass (m_w^*) for $0<|z|<l_0+t_w$, and by the barrier layer effective mass (m_b^*) otherwise.

The energy levels of a quantum well of thickness l can be obtained numerically from [42]:

$$l\left(E_{n_z}^{QW}\right)=\frac{2\hbar}{\sqrt{m_w^*E_{n_z}^{QW}}}\left[\tan^{-1}\left\{(-1)^{(n_z+1)}\left(\sqrt{\frac{m_w^*}{m_b^*}\left(\frac{V_0}{E_{n_z}^{QW}}-1\right)}\right)^{(-1)(n_z+1)}\right\}+\pi\times\text{int}\left(\frac{n_z}{2}\right)\right]. \tag{2-11}$$

The resulting spectrum consists only of discrete bound state energies. The shells are spaced evenly (intershell spacing of the order of tens of meV), and the intershell spacing decreases with increasing dot size. The number of bound states increases with increasing barrier height. As stated in section 2.1, the first bound state is filled up with two particles; the second bound state is filled after four particles and so on. This model does not take the effects of strain into account; more accurate models have been developed for lens-shaped dots [33] and for pyramidal dots [43].

In practice, however, the quantum dots obtained through the Stranski-Krastanow growth mode have potential barriers with finite heights, that is, at elevated temperatures carriers can escape the confined region by thermionic emission into the barrier material [44]. This important carrier-loss process is especially significant in structures with shallow barriers [45]. The carrier distribution between the active region (QD) and the confining layers (barrier and WL) is controlled by carrier thermalization/capture processes in the QD and the escape processes from QD to WL or barrier through thermionic emission. The probability per unit time for a carrier to absorb phonons and be emitted above the barrier is greatly enhanced at high temperatures due to a large phonon population in the lattice. Consequently, quenching of the emitted light intensity is observed at higher temperatures according to an exponential law of the form

$$I(T) = \frac{c}{1 + \alpha \exp\left(-E_A / k_B T\right)} , \qquad (2\text{-}12)$$

where c and α are adjustable parameters, $k_B T$ is the thermal energy, and E_A is the activation energy which corresponds to the minimal energy necessary to promote carriers to unbound energy levels. The onset of thermionic emission depends on the values of α and E_A.

2.4 Interband transition selection rules

Due to their discrete energy states, the transitions between the electron and hole levels in QDs are analogous to those between the discrete levels of individual atoms. The band-to-band transition probability per unit time is given by Fermi's golden rule. In the case of the creation of a photon [46]:

$$P_{if} = \frac{2\pi}{\hbar}\frac{e^2 F^2}{4m_0^2\omega^2}\left|\langle f|\,\mathbf{e}\cdot\hat{\mathbf{p}}\,|i\rangle\right|^2 \delta\left(E_i - E_f - \hbar\omega\right), \tag{2-13}$$

where **e** is the light polarization vector and $\hat{\mathbf{p}}$ is the momentum operator. The sum is over all the levels in the conduction and valence bands (initial states $|i\rangle$ and final states $|f\rangle$). E_i and E_f represent the energies of the initial and final states, $\langle f|\mathbf{e}\cdot\hat{\mathbf{p}}|i\rangle$ is the optical matrix element expressing the coupling between the initial and final states with the light polarization, and the term preceding the sum represents a constant of the system. Conservation of momentum and energy accompany emission and absorption of photons.

The reduced density of states observed in low-dimensional systems (compared to the usual bulk probability transitions) is introduced in the summation over initial and final states to account for dimensionality in the wavefunctions and the joint density of states. The electron and hole wavefunctions $\Psi_{i,f}(\mathbf{r})$ in low-dimensional systems are a product of the envelope function $\chi(\mathbf{r})$ and the appropriate Bloch function $u_{n\mathbf{k}=0}(\mathbf{r})$ at the Γ point, $\Psi(\mathbf{r}) \propto \chi(\mathbf{r})\, u_{n\mathbf{k}=0}(\mathbf{r})$. The matrix element in (2-13) can be factored into the integral over the unit cell of the fast varying part of the wavefunction (the Bloch function) and a sum at the cell centers $\mathbf{R}_i$ of the slowly varying functions (the envelope function).

The optical matrix element for transitions that involve an electron from a conduction band and a hole from a valence band is:

$$\langle f|\mathbf{e}\cdot\hat{\mathbf{p}}|i\rangle \approx \sum_{R_i}\chi_e(\mathbf{R}_i)e^{-i\,\mathbf{k}_e\cdot\mathbf{R}_i}\,\chi_h(\mathbf{R}_i)\,e^{i\,\mathbf{k}_h\cdot\mathbf{R}_i}\int_{\text{cell}} u_{ck_e}(\mathbf{r})(\mathbf{e}\cdot\hat{\mathbf{p}})\,u_{vk_h}(\mathbf{r})\,d\mathbf{r}\ , \quad (2\text{-}14)$$

where e and h represent electrons and holes and the integral is over unit cells. The electron and hole wave vectors are designated as $\mathbf{k}_e$ and $\mathbf{k}_h$. The exponential factors give a null contribution unless $k_e = k_h$, which is the vertical transition rule since light has negligible momentum. When factoring the electric-dipole matrix element in equation (2-13), the change in parity of electric-dipole transitions appears in the Bloch integral matrix element; this is just the same as in bulk systems.

The other selection rules have two origins: the overlap integral between envelope functions selects the quantum numbers of the initial and final level and the atomic-like dipole matrix element imposes the selection rules on polarization of the light wave. The atomic-like part of the Bloch wavefunction is similar for all III-V materials and the polarization selection rules are not dimensionality dependent.

The matrix elements for the envelope functions are integrals over their product with no polarization dependence. If the electron and hole quantum dot potentials are symmetric, the envelope functions could be symmetric or antisymmetric and their matrix elements will vanish unless both have the same parity. If the potential in both conduction and valence bands can be modeled as a quantum box with infinite potential walls, then the two sets of envelope functions are identical and only transitions between levels with the same index are allowed, this is the "$\Delta n = n - m = 0$" rule, where m is a valence-band state and n is a conduction-band state. In the case of lens-shaped dots, quantum dot wavefunctions have to be used, which for the first few levels can be approximated by in-plane harmonic functions [40]. For this case, the rule changes to "$\Delta n_x = n_x - m_x = 0$" and "$\Delta n_y = n_y - m_y = 0$". Also, the envelope functions are not exactly orthogonal since the effective depth of the confining potential is different for electrons and holes. This can lead to observations of transitions between $n \neq m$ states. These transitions will have weak intensities, and in order to conserve parity, $n - m = odd\ integer$ will only appear in the case of highly asymmetric potentials.

2.5 Heterostructure lasers

Electrically injected carriers in a *p-n* junction can recombine both radiatively and nonradiatively. The radiation originating from the recombination of carriers can interact with valence electrons and be re-absorbed, or interact with electrons in the conduction band to stimulate an identical photon. When the injected carrier concentration becomes large enough, the stimulated emission can exceed the absorption so that optical gain occurs. In order to sustain stimulated emission, a portion of the radiation must be reflected back to the laser medium. This way, the power gain due to amplification is at least equal to the total losses, including that of the oscillator output.

In the present work, separate confinement heterostructures are used to provide localized gain. The inner junctions or heterojunctions are used for carrier confinement and the outer heterojunctions are used for optical confinement. In Fabry-Perot laser cavities, cleaved facets act as a pair of reflectors and thus form the resonant cavity. A stripe electrode is used in order to restrict the injected current to a given width (figure 2.6).

The theory developed by Lasher and Stern [45] to analyze the interaction between electrons and light in semiconductor lasers is presented in section 2.5.1. Calculations based on this model performed by Arakawa and Sakaki [4], and by Asryan and Suris [48] for QD and QW lasers are summarized. In section 2.5.2, the multiple waveguide model is explained as well numerical analysis results of the samples studied are presented.

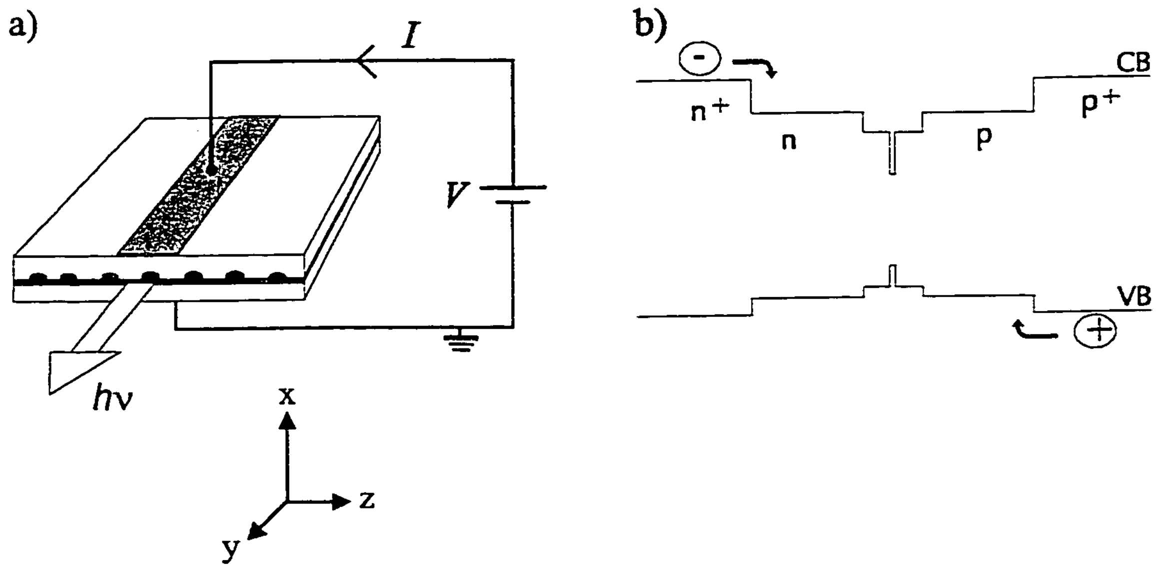

Figure 2.6 Schematics of (a) the geometry and (b) the diagram of conduction band (CB) and valence band (VB) of a heterostructure laser diode based on self-assembled quantum dots. The electrons (-) and holes (+) are injected in the active region with a forward bias voltage (*V*) and current (*I*).

2.5.1 Stimulated emission

The threshold current density of a semiconductor laser can be obtained from the recombination rate equations [47]. Electrons (holes) cascade down (up) the quantum dot potential by phonon emission and/or thermalize by electron-electron (hole-hole) interaction. Considering electrons in the limit of strong electron-electron interaction, i.e. under strong carrier injection such as for lasing conditions, a Fermi-Dirac distribution is established:

$$f_c(E) = \frac{1}{1 + \exp[(E - F_c)/kT]}, \qquad (2\text{-}15)$$

where E is the energy measured from the conduction band edge E_c, F_c is the electron quasi-Fermi level measured from the edge of the conduction band, k is Boltzmann's constant, and T is the temperature. The holes have a similar distribution function, f_v:

$$f_v(E-\varepsilon) = \frac{1}{1 + \exp[(E - \varepsilon - F_v)/kT]}, \qquad (2\text{-}16)$$

where ε is the photon energy.

With the densities of states obtained in section 2.2, and assuming $\Delta n = 0$ transitions, one can obtain the net rate of stimulated emission $r_{st}(\varepsilon)$, also called the gain coefficient, and the rate of spontaneous emission, $r_{sp}(\varepsilon)$. Using the "no k-selection rule" model of Lasher and Stern [48], one can obtain

$$g^{(i)}(\varepsilon) = r_{st}^{(i)}(\varepsilon) = \left(\frac{\pi^2 c^2 \hbar^3}{n_r^2 \varepsilon^2}\right) B^{(i)} \int_0^{\varepsilon - Eg} \mathrm{d}E \;\rho_c(E)\,\rho_v(E-\varepsilon)\,\{f_c(E) - f_v(E-\varepsilon)\}$$

(2-17)

$$r_{sp}^{(i)}(\varepsilon)=\left(\frac{\pi^2 c^2 \hbar^3}{n_r^2 \varepsilon^2}\right) B^{(i)} \int_0^{\varepsilon-E_g} \mathrm{d}E\ \rho_c(E)\rho_v(E-\varepsilon)\{1-f_c(E)f_v(E-\varepsilon)\} \quad , \tag{2-18}$$

where (i) stands for *0D* in quantum dots and *2D* in quantum wells, $B^{(i)}$ is a constant representing the probability of dipole transitions, E_g is the energy gap, c is the velocity of light, and n_r is the refractive index. The electron quasi-Fermi level is adjusted in such a way that the maximum gain $g^{(i)}(E)$ satisfies the threshold condition, i.e., $g^{(i)}(E_{max})$ is equal to the total optical loss in the laser cavity, which we assume to be independent of temperature. Because of the effects of the density of states, the spectral gain profile will be narrower for low-dimensional structures. The gain spectrum becomes discrete in the case of quantum dot lasers.

The rate $R_{sp}^{(i)}$ of the total spontaneous emission is calculated by the energy integral of the spontaneous emission rate

$$R_{sp}^{(i)}=\left(\frac{\pi^2 c^2 \hbar^3}{n_r^2 \varepsilon^2}\right) \int_0^{\infty} \mathrm{d}\varepsilon\ r_{sp}^{(i)}(\varepsilon)\ . \tag{2-19}$$

The rate equations for electron density, n, and number of photons, N_m, in the M^{th} lasing mode may be written as [49]:

$$\frac{\mathrm{d}n^{(i)}}{\mathrm{d}t}=\frac{J^{(i)}}{ed}+\frac{R_{sp}^{(i)}}{\eta}+\frac{m N_M^{(i)} r_{st}^{(i)}(\varepsilon_M)}{L_d W_d d \Phi(\varepsilon)} \tag{2-20}$$

$$\frac{\mathrm{d}N_M^{(i)}}{\mathrm{d}t}=-\frac{N_M^{(i)}}{\tau_M}+\frac{L_d W_d d R_{sp}^{(i)}}{M'}+\frac{N_M^{(i)} r_{st}^{(i)}(\varepsilon_M)}{\Phi(\varepsilon)}\ , \tag{2-21}$$

where d is the width of the active region, η is the quantum efficiency, L_d and W_d are the length and width of the device, τ_M is the photon lifetime in the lasing mode, and M' is the number of spontaneous modes. The number of modes per unit energy per unit volume is given by:

$$\Phi(\varepsilon) = \frac{n_r^3 \varepsilon^2}{\pi^2 \hbar^3 c^3} \ . \tag{2-22}$$

For simplicity one lasing mode is assumed (m = 1) and M' is very large so the second term of equation (2-21) is neglected. Under steady state condition, at the lasing threshold, the two rate equations (2-20) and (2-21) become:

$$J_{th}^{(i)} = \frac{e\,d\,R_{sp}^{(i)}}{\eta} \tag{2-23}$$

$$r_{st}^{(i)}(\varepsilon_M) = \frac{\Phi(\varepsilon)}{\tau_M} \ , \tag{2-24}$$

These two equations contain the two unknowns, $r_{st}^{(i)}(\varepsilon_M)$ and $R_{sp}^{(i)}$, which can only be solved when the two quasi-Fermi levels, F_c and F_v, are given. In general, the threshold current density is calculated numerically, but analytical expressions can be obtained for quantum well and quantum dot lasers as given by [4]:

$$J_{th}^{(2D)} = \frac{ed}{\eta}\frac{m_c}{\pi\hbar^2 l_z} p_0 B^{(2D)} kT \ln(1+Q)$$

$$\cong \frac{ed}{\eta}\frac{m_c}{\pi\hbar^2 l_z} p_0 B^{(2D)} kT \ln\left(\frac{m_v kT}{p_0 \pi\hbar^2 l_z}\right) \text{ (at high temperature)} \tag{2-25}$$

$$J_{th}^{(0D)} = \frac{ed}{\eta}\left(\frac{\alpha^{(0D)} V}{A^{(0D)}} + \frac{1}{V} - p_0\right) p_0\, B^{(0D)} \ , \tag{2-26}$$

where $V = l_x l_y l_z$, $A^{(i)} = \left(\frac{\pi^2 c^2 \hbar^3}{n_r^2 E_g^2}\right) B^{(i)}$, $Q = \left[\frac{\sqrt{C}D + (D-1)^{1/2}(1+C)}{1+C-CD}\right]^2$,

$D = \exp\left[\frac{\alpha^{(2D)}\left(\pi\hbar^2 l_z\right)^2}{A^{(2D)} kT m_c m_v}\right]$, $C = \left[\exp\left(\frac{p_0 \pi\hbar^2 l_z}{m_v kT}\right) - 1\right]^{-1}$, and m_c, m_v are the electron and hole effective masses, p_0 is the hole concentration in the laser active region, and $\alpha^{(i)}$ is the loss coefficient due to diffraction, free carrier absorption, etc. Equations (2-25) and (2-26) indicate that the threshold current density of a quantum well laser is proportional to $T\ln(T/\text{constant})$ near room temperature, whereas J_{th} of a quantum dot laser is independent of temperature.

Numerical calculations of J_{th} from the model described above have been performed for the GaAs/AlGaAs system [4] assuming that electrons populate only the ground state subband/sublevels, which is valid when l_x, l_y, l_z are sufficiently small. The results for T near room temperature are summarized in figure 2.7. They clearly show that the temperature dependence of J_{th} changes drastically with the degree of confinement of the carrier motion. In order to compare the temperature dependence of J_{th} for these devices, we express the results in terms of the conventional expression that is used to characterize semiconductor laser performance:

$$J_{th}(T_2) = J_{th}(T_1)\ \exp\left(\frac{T_2 - T_1}{T_0}\right). \qquad (2\text{-}27)$$

A high value of T_0 indicates relative temperature insensitivity for the laser device. Typical characteristic temperature values are T_0 = 120 – 160 K for a GaAs/AlGaAs double heterostructure laser diode operating at room temperature [50]. T_0 values obtained theoretically through this model for conventional double heterostructures, quantum well, quantum wire and quantum dot lasers are 104, 285, 481 °C, and ∞, respectively.

The reason for such a dramatic increase in T_0 can be understood as follows: for a conventional double heterostructure laser, the intrinsic temperature dependence of J_{th} (which is not related to a leakage over the barrier and Auger processes) is ascribed to the thermal spreading of the injected carriers over a wider energy range of states, which leads to decreases of the maximum gain $g(E_{max})$ at a given injection level. Consequently, in quantum well lasers, where the density of states of the electrons and the holes are step-like, the effect of such thermal spreading is expected to be smaller than in bulk-based lasers. In quantum dot lasers, the thermal spreading of carriers should vanish because the density of state is δ-function-like. Hence, the temperature dependence of J_{th} will totally disappear, as long as the electron population in the higher levels remains negligibly small.

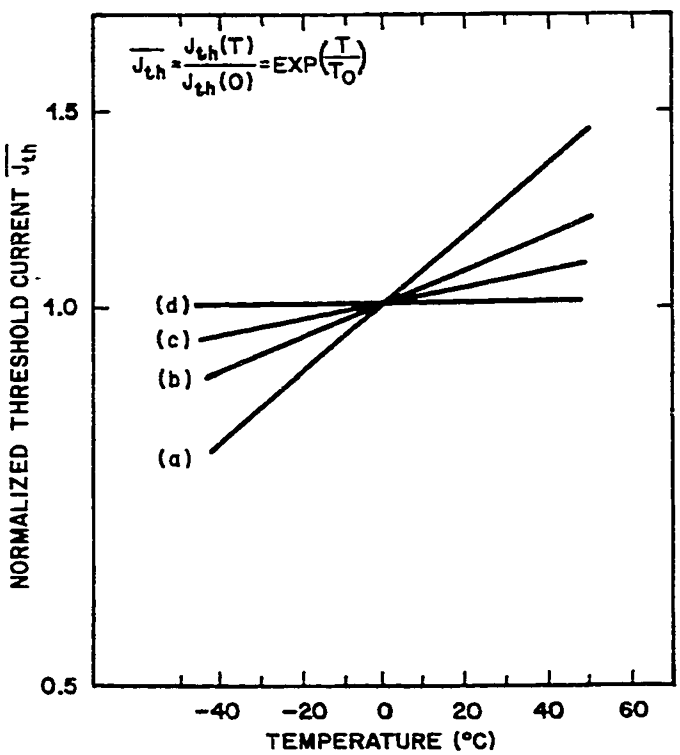

Figure 2.7 Numerical example of threshold current J_{th} calculated by extending the theory put forward by Lasher and Stern [48] for (a) a double heterostructure laser, (b) quantum well laser, (c) quantum wire laser, and (d) a quantum box laser [4].

The structures studied in this thesis have finite-height potential barriers and, as mentioned at the beginning of this chapter, the quantum dots have inhomogeneous broadened energy distributions. In the theoretical analysis of gain and threshold current of quantum dot lasers done by L.V. Asryan and R.A. Suris, these factors are taken into account [51]. Their analysis considers three variables: the operating temperature, the QD size fluctuations and the conduction and valence band offsets between the QD and barrier material.

In the case of relatively low temperatures and/or deep potential wells, the radiative lifetimes in QDs are small compared with the characteristic times of thermal excitation (escape) of the carriers from a QD (nonequilibrium filling of QDs). Having insufficient time to leave the QD, the carriers recombine within the dots and the threshold current density is essentially temperature independent as in the model described previously. The inhomogeneous broadening of the QD ensemble does not affect J_{th}.

When the system is at relatively high temperatures and/or the structure has shallow potential wells, equilibrium filling of QDs occurs. In this case, the characteristic times of thermally excited escapes of electrons and holes from the QDs are small compared with the radiative lifetimes in QDs. If the inhomogeneous line broadening $(\Delta E)_{inhom}$ is less than the temperature, J_{th} is found to be proportional to the square root of $(\Delta E)_{inhom}$. When the inhomogeneous line broadening is larger than the temperature, J_{th} increases linearly with increasing $(\Delta E)_{inhom}$.

These models assume that only the first quantized states (both in the conduction and valence levels) are involved in the transitions.

2.5.2 Optical waveguiding

For a laser to function, one needs an active medium for light amplification, QDs in the case of the samples studied for this thesis, and a resonating cavity, i.e. two mirrors delimiting a cavity capable of optical mode confinement such as a waveguide. The slab waveguide consists of a slab of high refractive index material sandwiched by low index material. Assume that light propagates in a guided medium along the y-direction. The light is confined in the z direction by the difference in refractive indices but diverges in the x-direction because there is no guiding structure in this direction (see figure 2.6a). Waveguiding in the x direction arises from the difference in gain between the regions underneath and outside the electrodes in Fabry-Perot lasers.

The guided light propagates along the y-direction with a sinusoidal time dependence (ωt, not explicit here) according to the wave equation [52]:

$$\nabla^2 E = k_0^2 \cdot n_r^2(x,y,z)\, E \quad , \qquad (2\text{-}28)$$

where the symbol E in the scalar theory represents the dominant component of the electromagnetic field, $k_0 = 2\pi/\lambda = \omega/c$, n_r is the index of refraction of the medium, and ω is the angular frequency. When n_r is y-invariant, the wave behavior can be described in terms of modes characterized by a constant of propagation and a y-invariant mode profile of the electric field $\psi(x,z)$:

$$E(x,y,z)=\sum_j c_j \psi_j(x,z)\cdot e^{i\beta_j z} + \int_{-\infty}^{+\infty} C(\nu)\psi_\nu(x,z)\cdot e^{iB(\nu)z}\,\mathrm{d}\nu \ . \qquad (2\text{-}29)$$

The lower case letters refer to the guided modes, while the uppercase represents the continuum of radiation modes that are necessary to take into account the part of the light energy that is not guided in the waveguide. These modes decay very rapidly with y since the continuous function $B(\nu)$ is imaginary.

If we consider only the guided modes (y-invariant in profile by definition), we obtain:

$$\nabla_\perp^2 \psi + k_0^2 \cdot n_r^2 \cdot \psi = \beta^2 \cdot \psi \ . \qquad (2\text{-}30)$$

The symbol $\perp$ is used to indicate that the derivatives include only the direction perpendicular to y and β is the propagation constant. This simplified equation is used to determine the mode profiles in conjunction with the appropriate electromagnetic field boundary conditions. These solutions are obtained numerically since only simple waveguide cases can be treated analytically [53]. In order to obtain the condition of total internal reflection inside the waveguide, the core material must have a larger index of refraction than the cladding material. Eigenmodes of the system must satisfy the equation above, both in the x and z directions. The modes have well-defined field distributions in the transverse x and z directions (transverse modes) and propagation constants in the y direction which are determined by the standing wave condition. The field intensity is the density probability of photons. A similar analysis can be done for the magnetic field $\boldsymbol{H}$.

Modeling of the eigenmodes for the lasers in this study was done using the multilayer slab guide model [54]. This technique is used when the slab waveguide structure has many layers. The analysis of multilayer stacks starts with the theory explained above as well as Maxwell's equations and defines two field variables U and W by

$$U = E_x \qquad , \qquad W = \omega \mu H_y \tag{2-31}$$

which describe the transverse variation of the optical field. Here μ represents the permeability constant. These definitions are chosen because $U(z)$ and $W(z)$ are quantities that are continuous at the layer boundaries. From solutions of Maxwell's equations for planar guides, we obtain the relations

$$U' = -jW \tag{2-32}$$

$$W' = j\left(\beta^2 - n_r^2 k^2\right) U \ , \tag{2-33}$$

where the prime indicates differentiation with respect to z, and j is equal to $\sqrt{-1}$. Both U and W obey the transverse wave equation

$$U'' = \left(\beta^2 - n_r^2 k^2\right) U \ . \tag{2-34}$$

U and W describe the transverse field distribution in a particular layer of constant refractive index n_r. The general solution of the wave equation in this layer is

$$U = A \ \exp(-\mathrm{j}\kappa x) + B \exp(\mathrm{j}\kappa x) \tag{2-35}$$

$$W = \kappa \left[A \exp(-\mathrm{j}\kappa x) - B \exp(\mathrm{j}\kappa x) \right] , \tag{2-36}$$

where the wave number κ is defined as

$$\kappa^2 = n_r^2 k^2 - \beta^2 \ , \tag{2-37}$$

The constants A and B can be replaced by the input values $U_0 = U(0)$ and $W_0 = W(0)$ at the input plane $z = 0$ of the layer. We obtain

$$A = \frac{1}{2}(U_0 + W_0 / \kappa) \tag{2-38}$$

$$B = \frac{1}{2}(U_0 - W_0 / \kappa) \ . \tag{2-39}$$

A rearrangement of (2-35) – (2-39) leads to a simple matrix relation between the output quantities U, W and the input quantities U_0, W_0

$$\begin{pmatrix} U_0 \\ W_0 \end{pmatrix} = \mathbf{M} \begin{pmatrix} U \\ W \end{pmatrix} , \tag{2-40}$$

where the pairs (U_0, W_0) and (U, W) have been written as vectors, and **M** is the characteristic matrix of the layer. It has the form

$$\mathbf{M} = \begin{vmatrix} \cos(\kappa x) & (\mathrm{j}/\kappa)\sin(\kappa x) \\ \mathrm{j}\kappa \sin(\kappa x) & \cos(\kappa x) \end{vmatrix} . \tag{2-41}$$

Note that det **M** = 1.

Now consider a stack of n layers sandwiched between a substrate and a cover. The layer thicknesses are h_i (labeling the layers starting from the cover) and the layer indices are n_i, where $i = 1$ to n. The output field variables for each layer are U_i and W_i. The characteristic matrices for the layers are

$$M_i = \begin{vmatrix} \cos(\kappa_i h_i) & (\mathrm{j}/\kappa_i)\sin(\kappa_i h_i) \\ \mathrm{j}\kappa_i \sin(\kappa_i h_i) & \cos(\kappa_i h_i) \end{vmatrix} , \tag{2-42}$$

where

$$\kappa_i^2 = n_i^2 k^2 - \beta^2 \ . \tag{2-43}$$

The corresponding field variables are related by

$$\begin{pmatrix} U_{i-1} \\ W_{i-1} \end{pmatrix} = \mathbf{M}_i \begin{pmatrix} U_i \\ W_i \end{pmatrix} . \tag{2-44}$$

Using matrix multiplication, we obtain a simple relation between the input variables U_0, W_0 at the cover and the output variables U_n, W_n at the substrate

$$\begin{pmatrix} U_0 \\ W_0 \end{pmatrix} = \mathbf{M} \begin{pmatrix} U_n \\ W_n \end{pmatrix} , \tag{2-45}$$

where **M** is the characteristic matrix of the stack. The product of the individual layer matrices gives

$$\mathbf{M} \equiv \begin{vmatrix} m_{11} & m_{12} \\ m_{21} & m_{22} \end{vmatrix} = \mathbf{M}_1 \cdot \mathbf{M}_2 \cdot \mathbf{M}_3 \ldots \mathbf{M}_n \ , \tag{2-46}$$

where m_{11}, m_{12} etc. are the matrix element used in the analysis.

Numerical calculations were carried for the waveguide structure shown in figure 3.1. The change in index of refraction as a function of the laser structure cross section is displayed in figure 2.8a. The results demonstrate that the dominant guiding modes of the structure are the first transverse electric and transverse magnetic modes. Figure 2.8b displays the electric field intensity of the first guided mode. The narrowness of the field intensity testifies that the outer heterojunctions confine the photons well (owing to the large change in index of refraction between the $Al_{0.25}Ga_{0.75}As$ and the $Al_{0.70}Ga_{0.30}As$ regions). The lasing threshold current is influenced by the mode confinement factor ξ, which is the ratio of the optical power in the active layer to the total optical power

$$\xi = \frac{\int_{\text{QDs}} |E_x(z)|^2 \, dz}{\int_0^\infty |E_x(z)|^2 \, dz} . \tag{2-47}$$

If the structure shown in figure 2.8 has one stack of quantum dots (as sample *IIa* in chapter 3), the confinement factor for the dots is calculated to be ~ 0.5 %; i.e., there is a 0.5 % overlap between the optical mode and the QDs. For a laser structure having five stacked layers of dots with 7 nm spacer layers (sample *IIb* in chapter 3), the confinement factor increases to ~ 2.5 %. Quantum well laser structures have confinement factors ranging between 2 and 10 % since wells are usually thicker than QDs [55]. Furthermore, self-assembled QDs cover at most 50 % of the *x-y* plane ([32, 56, 57] and figure 3.3) compared with 100 % for QWs, thus resulting in lower confinement factors for these structures.

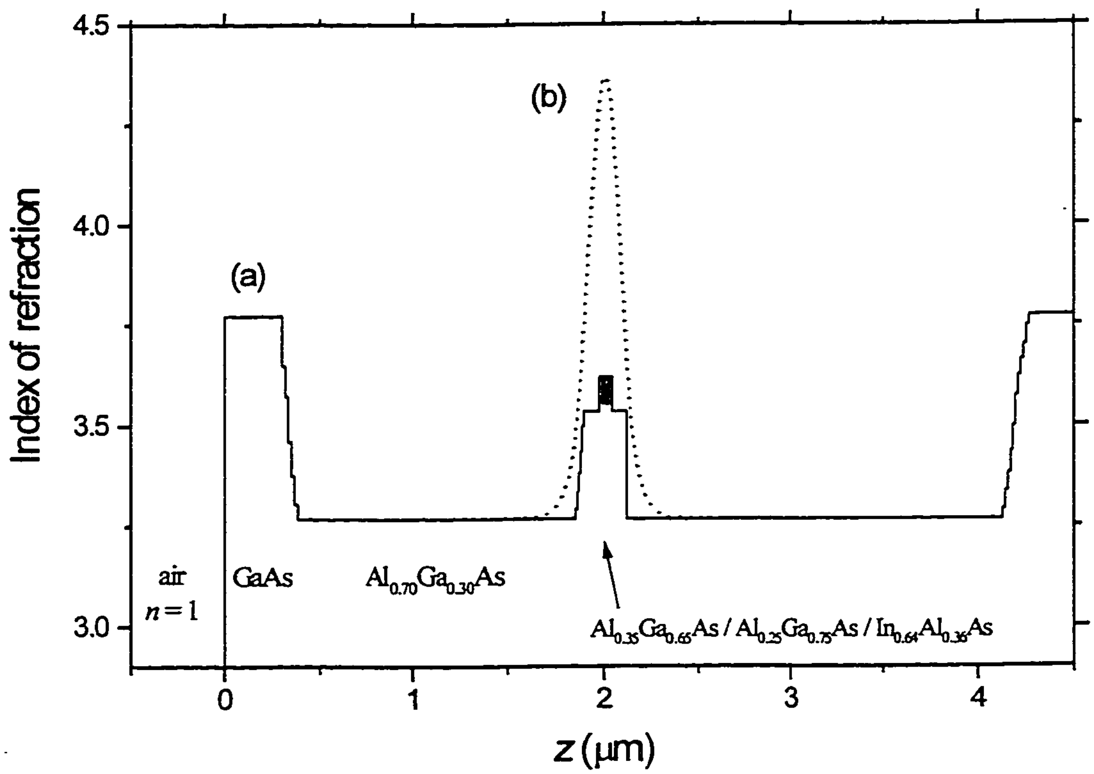

Figure 2.8 (a) Index of refraction as a function of the laser structure cross section for samples *IIa* and *IIb*. (b) The doted line represents the electric field intensity of the first guided mode in the quantum dot laser cavity. The cladding layers are symmetric on both sides of the active region.

2.5.3 Laser characterization

This section states the equations used for the characterization of laser properties presented in chapter 4.

The electrical input power P_{elec} provided to a laser structure is measured as $P_{elec} = R_s I^2$, where R_s is the sample resistance and I is the current delivered to the device. This resistance can be determined from a current-voltage (*I*-*V*) plot

$$R_s = \frac{\mathrm{d}V_s}{\mathrm{d}I} . \tag{2-48}$$

The device external quantum efficiency η_{ext} for stimulated emission is defined as the ratio of the rate of photons leaving the exit interfaces (2*P*,) to the rate of carriers crossing the junction [58], that is

$$\eta_{ext} = \frac{2P}{IV_s} , \tag{2-49}$$

where P is the output power from one facet of a laser. The factor 2 in equation (2-49) is included to account for light exiting from both facets. When one includes the power losses from the residual contact resistance, the above equation becomes

$$\eta_{ext} = \frac{2P}{IV_s - I^2 R_s} . \tag{2-50}$$

Equation (2-27) is used to characterize the threshold current as a function of temperature.

For current values above the threshold, many emission lines may be observed in the laser spectrum. These lines belong to the various longitudinal modes of the device, which can be amplified simultaneously. The basic mode selection in the *y*-direction (longitudinal direction) arises from the requirement that only an integral number m of half-wavelengths fits between the reflection plane. Thus

$$m\,\lambda = 2L_d\,n_r\,, \tag{2-51}$$

where L_d is the device length and n_r is the refractive index. The separation $\Delta\lambda$ between these allowed modes in the y direction is the difference in the wavelengths corresponding to m and $m + 1$. Differentiating the above equation with respect to λ, one obtains

$$\Delta\lambda = \frac{\lambda^2\,\Delta m}{2n_r\,L_d\left[1-(\lambda/n_r)(\mathrm{d}n_r/\mathrm{d}\lambda)\right]} \tag{2-52}$$

for large m. The term in brackets arises from dispersion.

Chapter 3

EXPERIMENTAL TECHNIQUES

This chapter details the samples studied and the experimental techniques applied. Initially a description of the different samples investigated with information on their growth, material composition and bandgap energies is given. Additional structural information, obtained from transmission electron microscopy, is discussed followed by some basic processing steps involved in the fabrication of broad area lasers. The last two sections present the fundamental theory and experimental implementation of the optical characterization employed: electroluminescence, photovoltage and photoluminescence.

3.1 Sample growth and preparation

All samples were grown by molecular beam epitaxy (MBE) on an *n*-doped GaAs (100) substrate. The Stranski-Krastanow growth mode was used to produce between one and five layers of QDs in the active region of a two-step separate confinement heterostructure (figure 3.1). The structures generally consisted of a thick (~2 μm) $Al_xGa_{1-x}As$ contact layer doped $n^+ \sim 6\times10^{17}$ cm^{-3}, followed by a bottom cladding layer of $n \sim 3\times10^{16}$ cm^{-3} doped $Al_yGa_{1-y}As$. The active region is composed of 15 nm undoped

$Al_{0.25}Ga_{0.75}As$ on each side of the $In_{0.64}Al_{0.36}As$ QD layer. The symmetric *p*-doped step-graded cladding and contact layers with corresponding doping and material concentrations follow and a 300 nm p^+-GaAs cap (p ~ 3×10^{19} cm^{-3}) terminates the

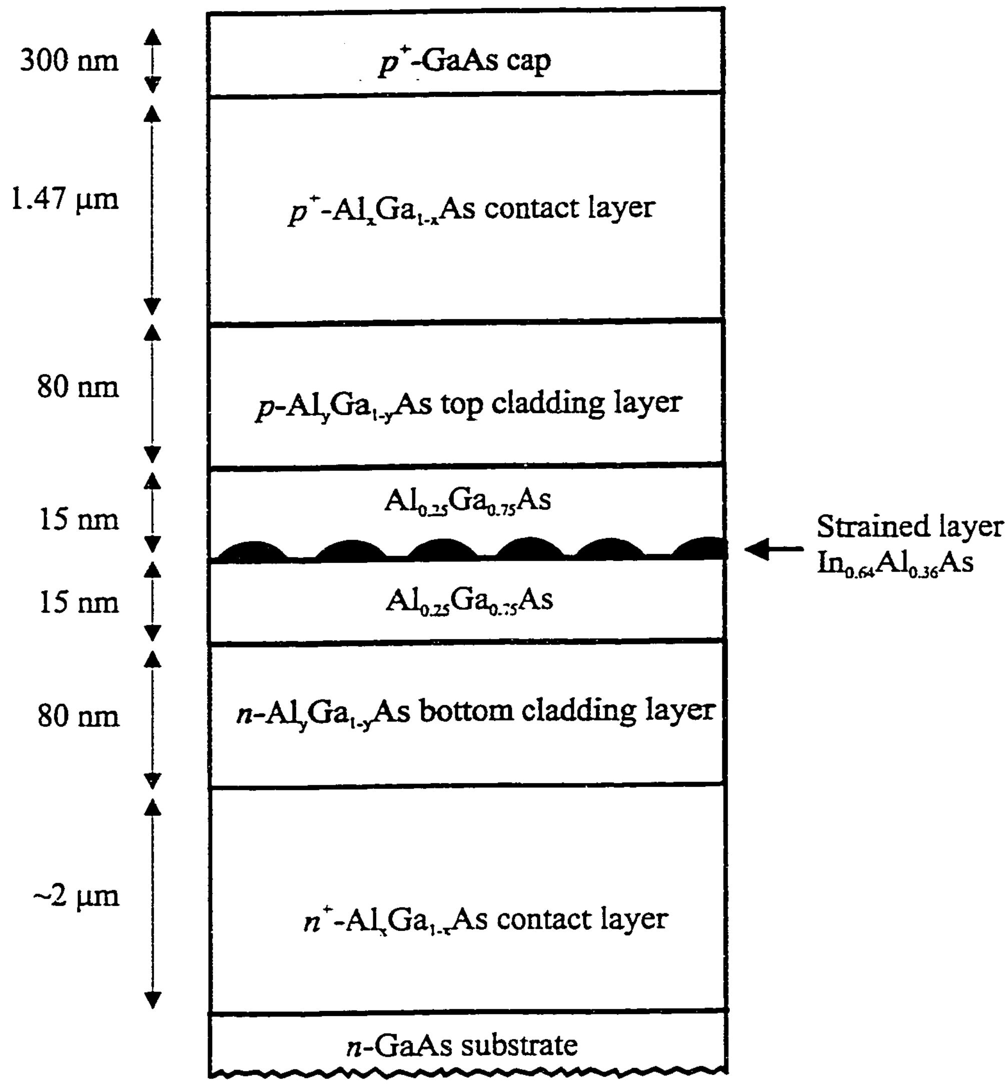

Figure 3.1 Cross-sectional view of the QD laser structure.

structure. Silicon was used for the *n* doping, while beryllium was employed for the *p* doping. The entire structure was deposited at T ~ 630 °C, with the exception of the QD section deposited at ~ 530 °C. Growth was interrupted for 2.5 minutes after the deposition of the QD layer; this growth interruption is arbitrary but important since in some strained systems, an evolution of the QD characteristics such as narrowing of the size distribution and lowering of the dot density is observed after material deposition [59, 60].

Table 3.1 enumerates the specific material compositions of six samples grown using this procedure. Sample *Ia*, *Ib*, *Ic* and *III* were fabricated at the National Research Council Canada using a modified V80H VG-Semicon MBE system, while samples *IIa* and *IIb* were rendered at Nortel Technology using a V80H VG-Semicon MBE system.

Sample	Description	Deposited amount of $In_{0.64}Al_{0.36}As$	Cladding layer $Al_yGa_{1-y}As$	Contact layer $Al_xGa_{1-x}As$
Ia	Single layer	4.5 ML	y = 0.30	x = 0.33
Ib	Single layer	2.5 ML	y = 0.30	x = 0.33
Ic	Single layer	2.0 ML	y = 0.30	x = 0.33
IIa	Single layer	5.0 ML	y = 0.35	x = 0.70
IIb	5 layers of dots with 8 nm $Al_{0.25}Ga_{0.75}As$ spacer layers	4.5 ML	y = 0.35	x = 0.70
III	Unstrained 5.0 nm thick GaAs QW	———	y = 0.35	x = 0.70

Table 3.1 Material composition of the various lasers studied. ML stands for monolayer.

Samples *Ia-c* are all single QD layer laser structures with different amounts of deposited material. They are used to study the emission characteristics of the QDs, wetting layers and barriers. Samples *IIa&b* have an improved carrier confinement resulting from the higher potential barriers (figure 3.2). *IIb* is used to study the laser properties observed when more than one stack of layers is present in the active region. Sample *III* is a reference GaAs/AlGaAs QW laser. The confining potentials are drawn in figure 3.2 for samples *I* and *II* [61-63]. Table 3.2 displays the bandgap energies and conduction band offsets of the different materials contained in the heterostructures. The conduction band offsets (ΔV) correspond to ~ 70% for AlInAs/AlGaAs systems and ~ 65% for AlGaAs/GaAs based systems [64, 65]. The lattice mismatch between $Al_{0.36}In_{0.64}As$ and $Al_{0.25}Ga_{0.75}As$ is ~ 3.2 % [63, 66]; this tensile strain produces a decrease in the bandgap compared with unstrained materials.

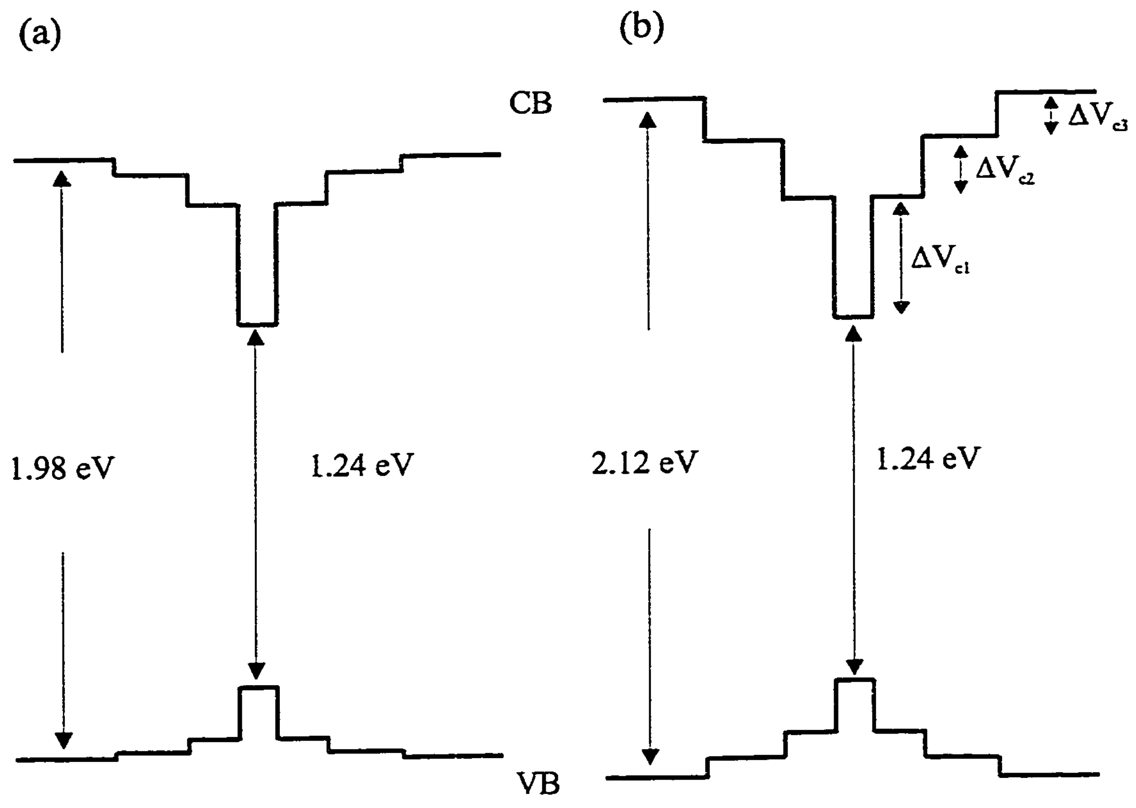

Figure 3.2: Schematic energy-band diagram of (a) samples *Ia-c*, and (b) samples *IIa&b*.

Samples	Active layer E_g	Buffer layer $Al_{0.25}Ga_{0.75}As$ E_g	Cladding layer $Al_yGa_{1-y}As$ E_g	Contact layer $Al_xGa_{1-x}As$ E_g	ΔV_{c1}	ΔV_{c2}	ΔV_{c3}
I	1.24	1.87	1.94	1.98	0.42	0.047	0.027
II	1.24	1.87	2.00	2.12	0.42	0.087	0.08
III	1.42	1.87	2.00	2.12	0.29	0.087	0.08

Table 3.2: Bandgaps and conduction band offsets at room temperature in eV. The QD and contact layer bandgap values do not include the effects of strain.

To measure the QD structural characteristics of the various samples, cross-sectional transmission electron microscopy (TEM) was performed. Figure 3.3 reveals samples having a high density of InAlAs islands, with a base diameter of ~ 20 nm and a thickness of ~ 5.0 nm. The WLs have a thickness of 2-3 nm. These structural characteristics are comparable to the ones obtained with similar self-assembled dots where other fundamental studies were performed [67, 68]. Figure 3.3c shows the cross-sectional TEM of sample *IIb*, where the 5 stacks are clearly observed and demonstrate vertical self-alignment of the dots caused by the interacting strain fields induced by the dots which give rise to a preferred direction in the In migration [69, 70]. The dot dimensions increase in the upper layers in a correlated growth regime. This vertical self-assembling is only observed in samples were the spacer layers are thin (less than ~ 30 nm) [69].

The TEM micrographs also show that the growth front returns to a planar mode after only a few nanometers of deposited $Al_{0.25}Ga_{0.75}As$ above the quantum dots to produce an atomically flat interface at the upper $Al_{0.25}Ga_{0.75}As/Al_yGa_{1-y}As$ heterojunction. The estimated dot dimensions and densities obtained from the cross-sectional TEMs are displayed in table 3.3. Sample *Ia*'s TEM micrograph QD features were not clear enough to allow quantification of the QD density.

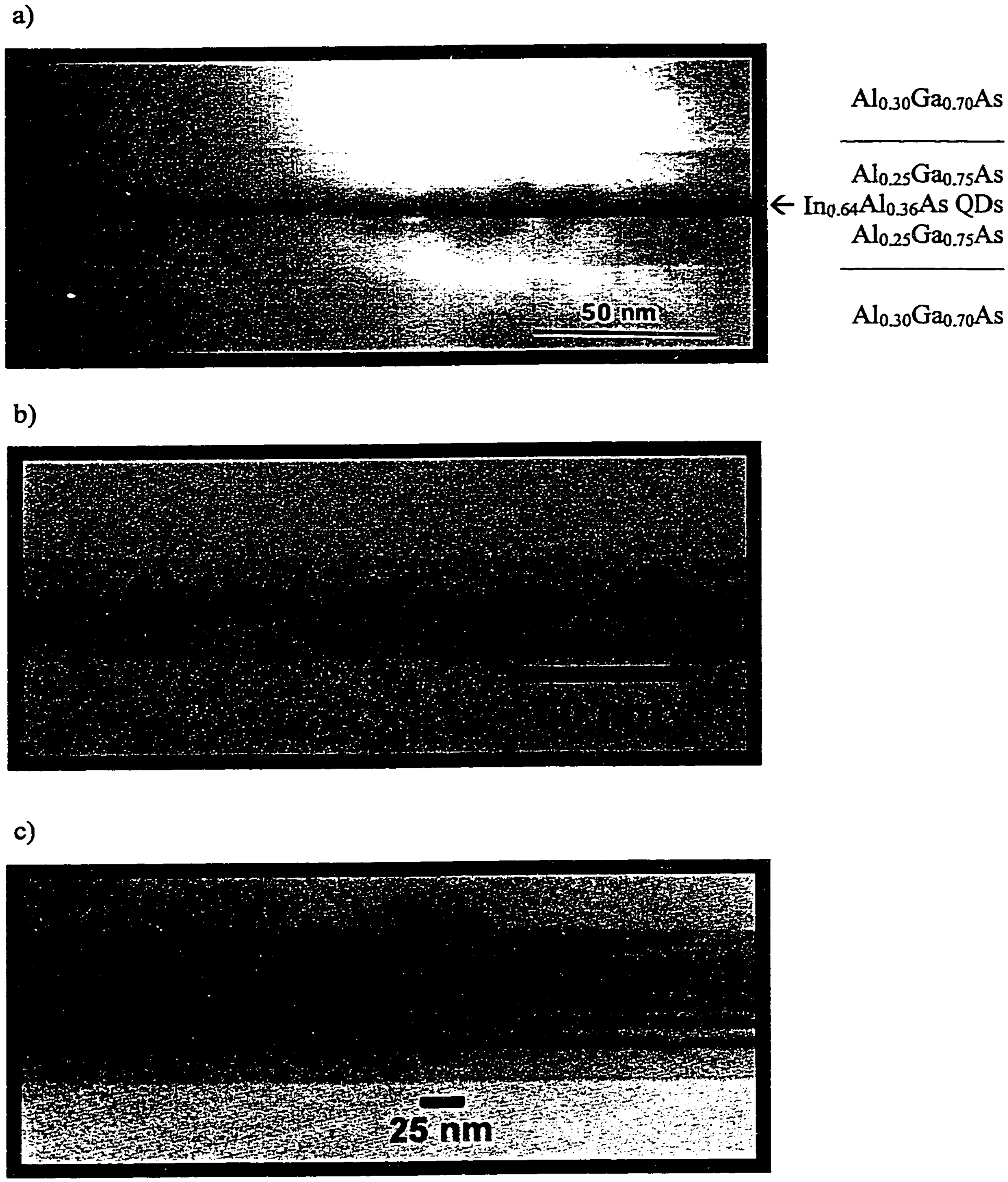

Figure 3.3: TEM cross-section view of the active region of the samples, which reveals the $Al_{0.36}In_{0.64}As$ QDs (dark) at the center of the $Al_{0.25}Ga_{0.75}As$ (pale), and with the $Al_{0.25}Ga_{0.75}As/Al_yGa_{1-y}As$ interface (line above and below). (a) Sample *Ia* with 4.5 ML of deposited material, (b) sample *IIa* with 5.0 ML, and (c) sample *IIb*, the stack of 5 QD layers with 4.5 ML deposited.

Sample	QD density (dots/μm^2)	Average QD base diameters (nm)	QD heights (nm)
Ia	Not measured	~ 20	6.3 ± 1.0
IIa	500 ± 200	~ 20	5.5 ± 1.0
IIb	2500 ± 1000	~ 15 - 36	~ 3 - 4

Table 3.3 Estimated QD dimensions obtained from cross-sectional TEM aspect ratio measurements.

Secondary ion mass spectroscopy (SIMS) analysis was performed on sample *IIb*. Doping level results showed beryllium diffusion, the *p*-dopant used, all the way through the intrinsic region. This dopant diffusion in the active region was expected to affect the performance characteristics of the lasers, and therefore the intrinsic region was widened in the subsequent growth of sample *IIa* (*IIb* was grown before *IIa*).

The laser structures were processed into broad area lasers with two cleaved uncoated facets to form a laser cavity. A ~ 2 cm^2 wafer piece was cleaned using organic cleaners, hydrochloric acid, and ammonium hydroxide. The *p*-doped side of the structure was coated in photoresist with a stripe pattern mask over it, which was then exposed to ultraviolet light and subsequently etched, leaving only the stripe design. After this, 25 nm of titanium, 55 nm of platinum, and 300 nm of gold were evaporated onto the sample, and this was followed by a metal lift-off. The metal stripes were used as the positive electrical contacts during the experiments; these had widths of 40, 60, 100, 150, and 200 μm. At this point, the metals used to protect the semiconductor material beneath them, the top 0.6 μm of GaAs, and the AlGaAs *p* layers were etched away. This etch prohibits current spreading along the lateral direction of the laser. The GaAs substrate was then thinned from 600 μm (samples *IIa* and *IIb*) or 450 μm to ~ 150 μm for easy cleaving, and 25 nm of nickel, 55 nm of germanium, and 80 nm of gold were evaporated at the base of the sample and were used as the negative electrical contact. The processed samples were cleaved into 400 μm-1250 μm wide strips, and each strip holding 5-10 broad area lasers. The strips were then bound on laser diode mounts with a thermally activated, electrically conducting epoxy which provided the negative contact, while gold bonding of the top metallization strip provided the positive contact.

3.2 Electroluminescence

In electroluminescence (EL), electrons and holes are injected electrically into a sample and emit a photon after recombination. In a quantum dot laser structure, the carriers are injected into the barrier material, and diffuse to the vicinity of the quantum dots. At this point, the carriers thermalize through phonon emission and/or carrier-carrier (Auger) interaction from a continuum of barrier states, to the WL, and subsequently to the discrete states of the quantum dots where they eventually recombine radiatively. Band-to-band recombination follows the selection rules stated in section 2.4. This was the main technique utilized to characterize the samples since electrical injection experiments provide very clear results in many layered heterostructures.

Figure 3.4 illustrates an EL set-up. The sample was placed in an optical cryostat that kept its temperature constant and allowed for electrical contacts. Under forward bias, electrons and holes were injected electrically into the semiconductor laser where they recombined in the active region producing photons. The luminescence was collimated and focussed by a lens system into the entrance slit of a spectrometer. The emitted light spectrum was then dispersed by a grating and detected with an appropriate photodetector. The detected signal was digitized and stored in a computer.

The typical apparatus consisted of a liquid helium-cooled optical cryostat equipped with a heater and temperature controller for measurements between $T = 5$ K and $T = 300$ K with an uncertainty of ± 2 K, or a liquid nitrogen-cooled optical cryostat for measurements at $T = 77$ K. The QD lasers were excited using a Hewlett Packard 214B pulsed power supply driven at a frequency of 100 Hz and having 10 μsec square pulse widths. Voltages were measured using a Tektronix TDS 320 oscilloscope. The inset in figure 3.4 shows the electrical circuit employed to measure the potential difference. The samples in the cryostats were mounted on a cold finger in thermal contact with the cooling liquid.

In the case of the helium-cooled cryostat, a 0.66-m spectrometer equipped with a 600-grooves/mm grating dispersed the light onto a Spectrum One CCD array by SPEX Industries. The CCD array used a parallel detection scheme with a window range of 118 nm over 1024 pixels when using the 600-groves/mm grating. A luminescent line having a FWHM of 3 pixels on the CCD detector leads to a spectral resolution of 0.35 nm, which translated to an energy resolution of 0.9 meV at 700 nm.

In the case of the liquid nitrogen-cooled cryostat, a 0.67-m spectrometer was used with a United Detector Technology PIN 10D Si photodiode for strong luminescence signals and a Hamamatsu R928 photomultiplier tube for weaker signals. A dispersion of ~ 1.2 nm/mm was obtained with a 1200 grooves/mm grating, giving an energy resolution of 3 meV at 700 nm. The signal was analyzed with the help of a Stanford Research Systems SR810 DSP lock-in amplifier. The uncertainty on the detected signal is determined by evaluating the intensity changes in a part of the spectrum that has no features. This would correspond to a random uncertainty of ± 0.05 on the noisy spectrum in figure 4.1 and to values equivalent to the trace width in figure 4.3.

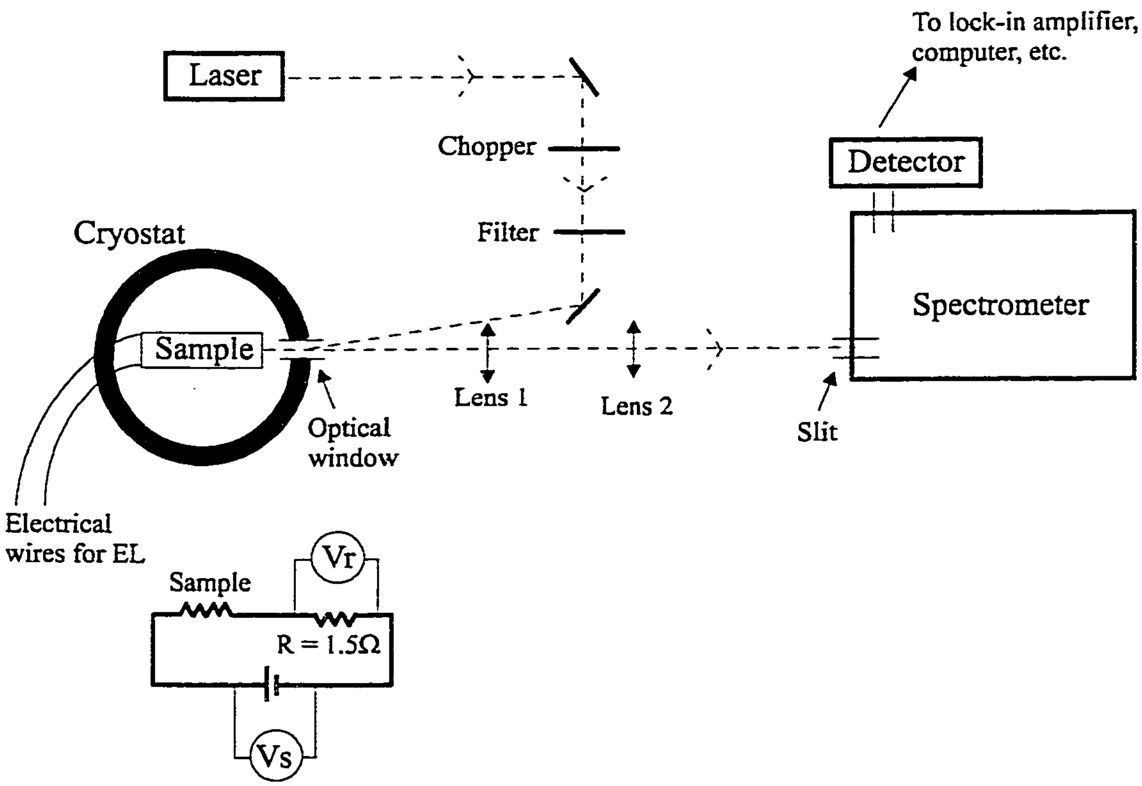

Figure 3.4 Experimental set-up for electroluminescence and photoluminescence. Shown at the bottom of the figure is the electrical circuit used for powering the QD lasers.

For the lasing output characteristics of the devices, a Newport 840 optical power meter was placed at the exit window of the cryostat. This allowed the measurement of the total output power as a function of the current injected into the device. A systematic measurement uncertainty of ~ 10 % arises from a partial light reflection in the cryostat window and from a possible clipping of the laser beam due to the small window diameter. This uncertainty is not taken into account in the calculations. The residual contact resistance has an uncertainty of ~ 10 %. This value is obtained from the linear regression of the lasers I-V plots. The measurement uncertainty combined with the residual contact uncertainty results in systematic uncertainties of ~ 15 % on external efficiency values. The curve shape is still valid since random uncertainties due to electronic instruments such as oscilloscope, multimeters and power meter are less than 2-3 % total.

The uncertainty on the threshold current density is dominated by a possible current spreading along the lateral direction (*x-y*) of the metal gate and the effective laser width becomes greater than the actual gate width [50]. This systematic uncertainty can be estimated to be ~ 10 % and is not taken into account in the calculations. The random uncertainty due to electronic instrumentation can be estimated at less than 5 %.

3.3 Photovoltage and photoluminescence

Some of the samples where studied by photovoltage (PV) and photoluminescence. Photoluminescence is the radiative process by which a material emits a photon after recombination of thermalized photo-created electron-hole pairs. Photovoltage is a scanning technique sensitive to direct changes in the optical properties due to modifications in the absorption coefficient related to the various energy levels. This technique can give useful information on the quantum dots as well as higher energy levels from the wetting layer and the barrier materials.

The PV experimental set-up (figure 3.5) consisted of a tungsten filament light source dispersed with a spectrometer; the monochromatic beam exited the spectrometer, went through a chopper, and was focused with two lenses on the sample through one of the optical windows of the cryostat. The laser sample was used as a light detector, and the PV was measured by standard synchronous techniques. The measurements were done with equipment described in the electroluminescence section.

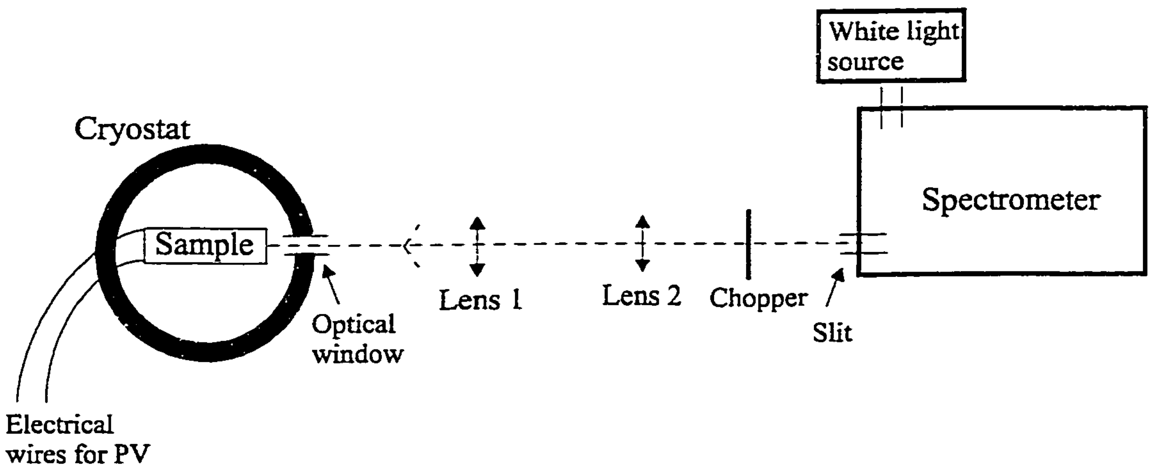

Figure 3.5 Experimental set-up used for photovoltage.

The experimental set-up used for PL was very similar to the EL set-up described earlier (see figure 3.4). In this case, a filtered laser beam, at an energy larger than the materials bandgap value, was used to excited the sample. Experiments were done with a continuous wave argon ion laser at $\lambda_{exc} = 514.5$ nm. For thick samples with a significant number of layered materials such as the ones studied here, PL spectra were often ambiguous since interference fringes were present due to the device waveguide configuration, and since luminescence intensities from the different material layers varied greatly depending on the position and angle of the incident laser light.

Chapter 4

RESULTS AND DISCUSSION

Electroluminescence spectra of samples with different deposited amounts of InAlAs are acquired to characterize the spontaneous and stimulated emissions originating from QDs, WL, and barrier material in the laser structures. In addition, the structures are verified using photoluminescence and photovoltage. A dependence on the confining potential for the temperature characteristic of the threshold current is observed when comparing samples with different barrier layer confining energies. The specific properties of multi-stack QD structures are shown and subsequently discussed. Operating characteristics of QD lasers, such as peak power output, external quantum efficiency and temperature dependence of threshold current density, are also presented. These results are systematically compared with control QW lasers.

4.1 Electroluminescence

The first part of this work provides experimental evidence that stimulated emission can be obtained from QDs. The three samples having different deposited amounts of InAlAs, but the same confining potentials: samples *Ia*, *Ib* and *Ic* are discussed in this section. Samples *Ia* and *Ib* were processed into 60 μm by 400 μm broad area lasers.

4.1.1 Spontaneous emission from quantum dots

As shown on the TEM in figure 3.3a, sample *Ia* has a relatively high QD density. If we assume a QD coverage of ~ 50% of the plane (which is roughly that estimated from the TEM cross section), the number of QDs which are present in the resonating cavity (60 μm × 400 μm) can be estimated at ~ 10^7. At $T = 77$ K, for very low injection currents, the EL emission of this sample is centered at a wavelength $\lambda = 725$ nm (1.711 eV) with a ~ 54 meV full width at half maximum (FWHM) Gaussian lineshape (figure 4.1). This emission spectrum is similar to the PL spectrum obtained with nominally equivalent QDs grown in an *n-i-n* structure designed for a separate optical investigation [71]. It is also comparable to the PL spectra obtained from self-assembled QDs displaying efficient photocarrier thermalization with no observable excited-state emission under low excitation intensity (figure 2.2). The inhomogeneously broadened Gaussian EL line shape is therefore attributed to the emission from injected carriers thermalized in the statistically distributed ground states of the probed QDs.

A closer look at figure 4.1 reveals a slight asymmetry in the EL peak broadening to higher energies indicating the possibility that some state-filling effects occur at very low injection current densities. As described in section 2.1, state-filling effects are due to the fact that only two carriers can populate the ground state level in a QD. Under low excitation intensities, only the ground state level of the QDs are populated owing to a fast intersublevel relaxation from the higher energy levels to the lowest energy level, leaving only radiative recombination from the QD ground states. As more carriers are injected into the QD structure, a progressive saturation of the QD ground states occurs, leaving the higher energy states populated. Therefore, under such high injection, radiative recombination from excited states is observed as the intersublevel carrier relaxation toward the lower level is slowed due to the reduced number of available final states [21, 35-37, 56]. If the inhomogeneous broadening were less than the intersublevel spacings, the state filling effect would give distinct peaks at high injection currents similar to the ones observed in figure 2.3. For these InAlAs QDs, the inhomogeneous broadening is larger than the inter-sublevel spacing, so the state filling effect produces a spectrum with an asymmetric peak shifting towards higher energies as the injection current is increased [9, 30].

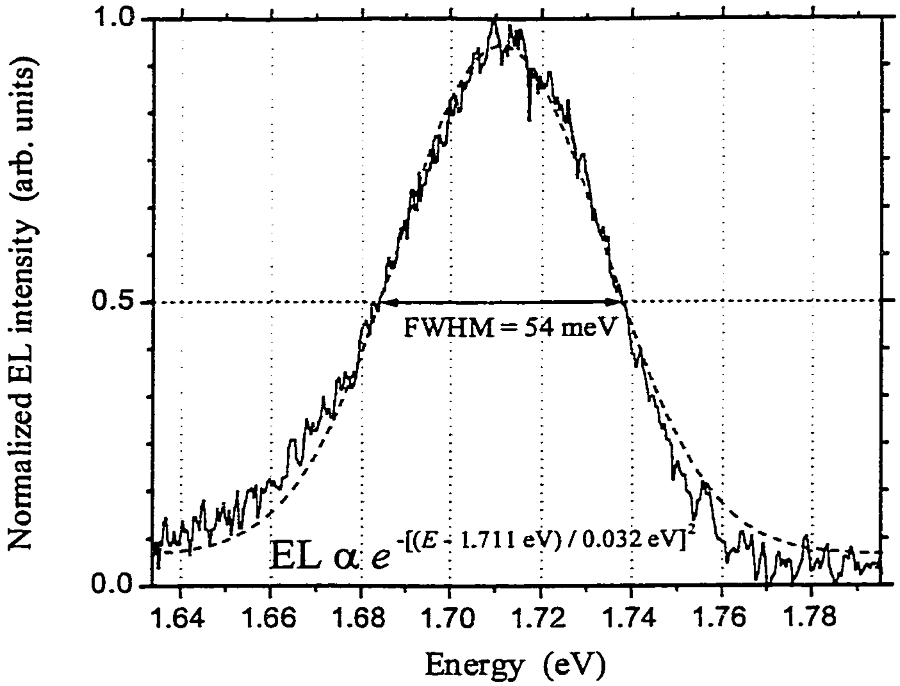

Figure 4.1 EL of sample *Ia* for very low bias ($J = 3$ A/cm^2) at $T = 77$ K.

When large ensembles of QDs are probed, it is not possible to observe the very sharp homogeneous EL emission line of each individual QD (see figure 2.3, p. 12) [37]. To reveal the intrinsic sharpness of the emission from each QD, we gated the structure with an opaque electrode having a small opening (a few square micrometers) in its center. The detected EL, which originates from a much smaller number of QDs, is shown in the high resolution EL-spectrum of figure 4.2 for various applied voltages. As observed, a number of sharp spectral features of comparable amplitudes appear with FWHM ranging from 200 to 500 μeV. Each sharp feature corresponds to the EL of a few QDs emitting at similar wavelengths. The small energy shift of individual lines (redshift) observed with increasing voltage can be attributed to the quantum-confined Stark effect [71]. The sharpness of the lines demonstrates the zero-dimensional nature of the energy levels in which the electrically injected carriers thermalize and recombine.

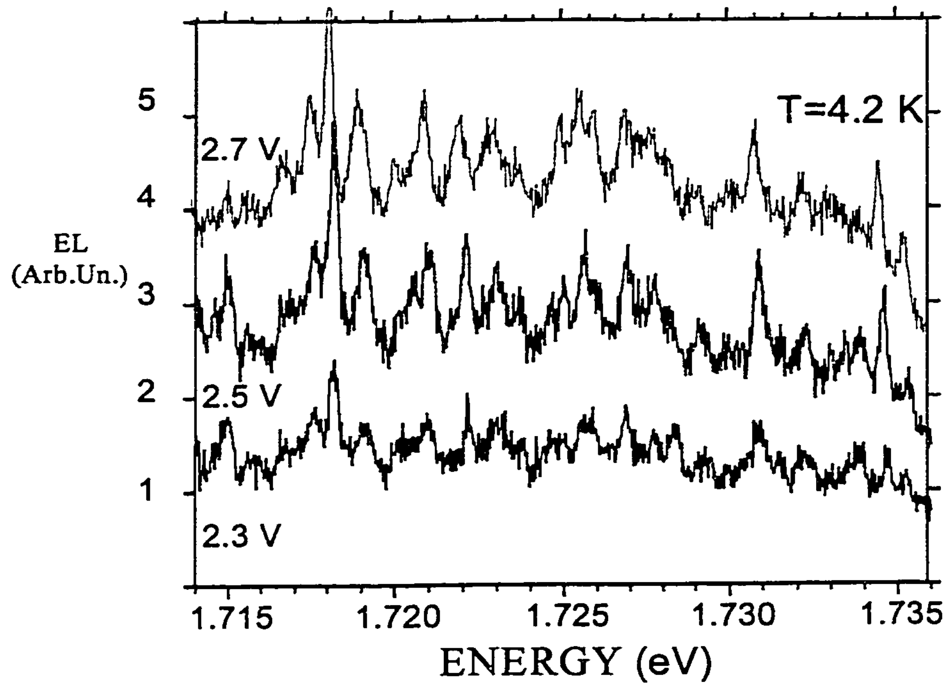

Figure 4.2 Low-temperature (4.2 K) EL spectra obtained at various applied voltages on sample *Ia* gated with an opaque electrode having an opening of a few square micrometers that is used to delineate the number of QDs probed. The sharp emission lines reveal the discrete nature of density of states of the individual dots.

4.1.2 Stimulated emission from quantum dots

The 77 K EL emission from a broad area laser structure under forward bias is shown in figure 4.3. For currents < 10 mA, the EL line shape is Gaussian and centered at 725 nm (lowest curve of figure 4.3a is the curve displayed in figure 4.1). With increasing current, the emission peak becomes asymmetric and shifts to higher energies. For currents just below lasing threshold, the spectral distribution narrows progressively and at ~ 175 mA (current densities $J \sim 700$ A/cm^2), a stimulated emission peak appears on top of the asymmetric EL peak. As the current is increased further, the laser cavity supports multiple longitudinal modes, and several sharp lasing peaks appear near 707 nm (1.754 eV). These can be seen more clearly in the semilogarithmic plot of figure 4.3b for a current of 600 mA ($J = 2500$ A/cm^2), and a peak laser output power of 44 mW. These wavelengths are in the far red spectrum and can be seen by eye. The output beam is spatially collimated and has a considerable divergence due to the very narrow active region. This stimulated emission is attributed to the QDs.

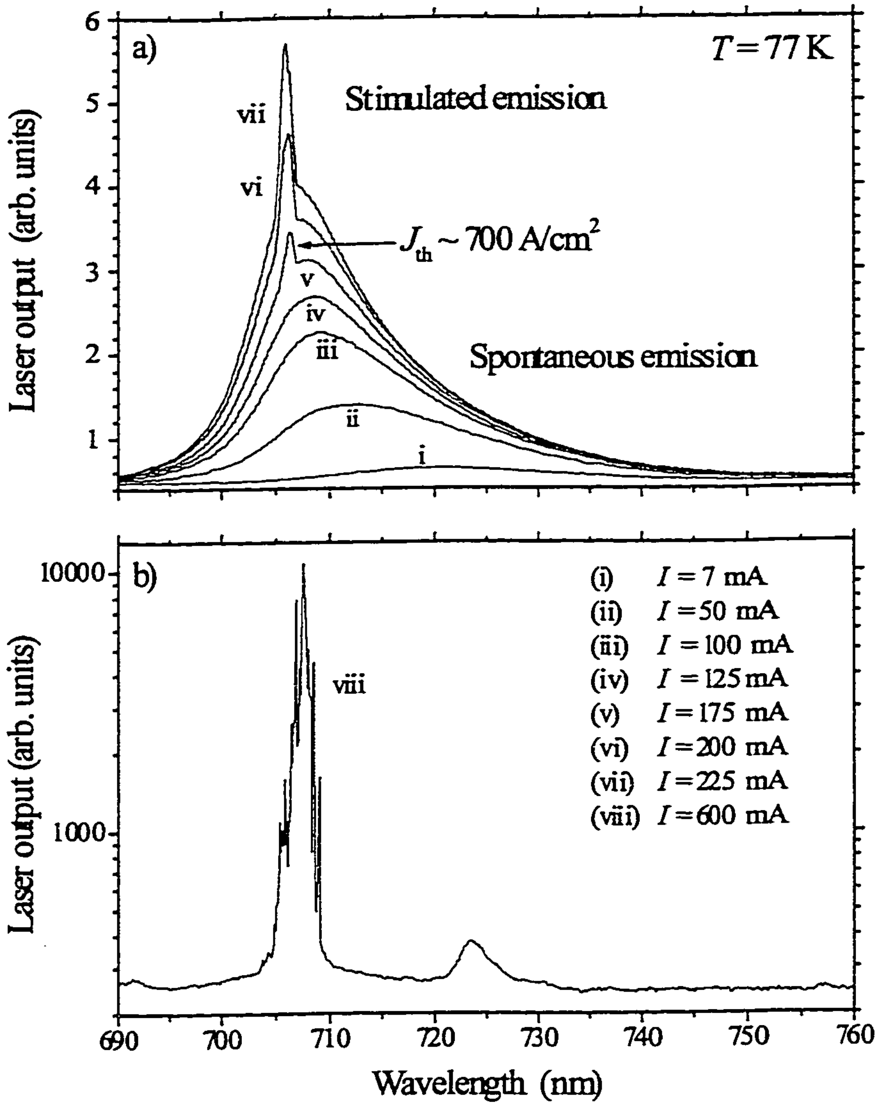

Figure 4.3 The (a) EL and (b) multimode lasing spectrum at 77 K of sample *Ia* for forward biases. The QD structure processed into a broad area laser emits in the red wavelengths (1.754 eV). The emission changes from spontaneous to stimulated as the injection current is increased above a threshold of 175 mA (J_{th} ~ 700 A/cm^2). The optical gain for the various lasing modes is provided by a different QD subset in the ensemble of ~ 10^7 QDs in which carriers are injected.

For each longitudinal mode, a different subset of the QD ensemble provides the optical gain. The ~ 40-meV blue shift observed between the low-current Gaussian EL spectra and the asymmetric spectra at threshold is most likely attributable to a change from emission from the QD ground states, at low current, to emission from the QD excited states, at threshold current where the larger number of injected carriers are filling the QD ground states. The 40-meV shift would then correspond to the sum of the electron and the hole intersublevel spacings between two adjacent allowed optical transitions. This is consistent with similar state filling effects observed in the PL spectra of QDs excited optically [9, 30, 31, 35, 60]. Furthermore, the small higher energy peak observed at λ = 724 nm (1.713 eV) under lasing conditions (figure 4.3b) matches the peak position of the ground-state emission that is observed at very low injection currents (lowest curve of figure 4.3a). Other lasers fabricated from the same wafer gave spectra equivalent to those presented in figure 4.3, including the weaker peak at λ = 724 nm in their lasing spectrum. This result suggests that the stimulated emission at 707 nm originated from the QD excited states and that the weaker peak at 724 nm originates from the filled QD ground states.

To obtain stimulated emission, each emitted photon on average must produce more than one stimulated photon before leaving the laser or being absorbed. The first QD sublevel is limited to two carriers, hence the photon production from ground state recombination in a QD laser structure may not be large enough for the power gain to exceed the losses. By increasing the injected carrier population, state filling effects occur, and radiative recombination from the second QD sublevels dominates the spectrum. These levels are doubly degenerate and permit a population of four carriers. More photons can be produced from the second level increasing the gain sufficiently to exceed the losses due to absorption in the amplifying medium and the power loss by transmission through the mirrors. Therefore, the larger degeneracy in a higher-order QD electron state can provide a larger optical gain compared with that of the ground state [72].

The luminescence properties of sample *Ia* can be compared with the emission from samples grown with the thinner strained $In_{0.64}Al_{0.36}As$ layers, samples *Ib* and *Ic*.

For sample *Ic* only 2 monolayers (ML) of $In_{0.64}Al_{0.36}As$ were deposited. As shown in figure 4.4a, the 5 K EL spectra for very low injection current displays spontaneous emission from a well-defined dominating quantum-well peak at $\lambda = 673$ nm (1.842 eV) having a 15 meV FWHM and a quantum dot emission peak at $\lambda \sim 718$ nm (1.727 eV). Even at such low current, the QD emission shape displays an asymmetric shift towards higher energies. The broad area laser structure based on this very thin quantum well produces stimulated emission at 5 K as shown in figure 4.4b and 4.4c. The lasing threshold injection current is roughly four times larger than that of the QD sample *Ia*. The stimulated emission originates from the bulk $Al_{0.25}Ga_{0.75}As$ at $\lambda = 658$ nm ($h\nu =$ 1.884 eV) just above threshold (830 mA, curve ii), but as the current is increased to 900 mA, lasing from both the bulk AlGaAs and the thin quantum well at $\lambda \sim 670$ nm (hν ~ 1.851 eV) is observed (curves iii and iv). For currents equal or greater than ~ 1.2 A, some weak residual QD emission was observed (curve v). This stimulated QD emission originates from excited levels in the dots since emission is centered about $\lambda = 699$ nm (1.774 eV), a 47 meV shift compared with the spontaneous emission peak centered at $\lambda \sim$ 718 nm for very low currents. For sample *Ic*, above lasing threshold, a gradual broadening of the spectral distribution is observed as the current is increased (from curve ii to curve iv in figure 4.4) as well as a sharp increase in the light output intensity which is characteristic of stimulated emission in semiconductor laser diodes. The fine structure observed in curve iv corresponds to longitudinal modes, where the long resonating cavity

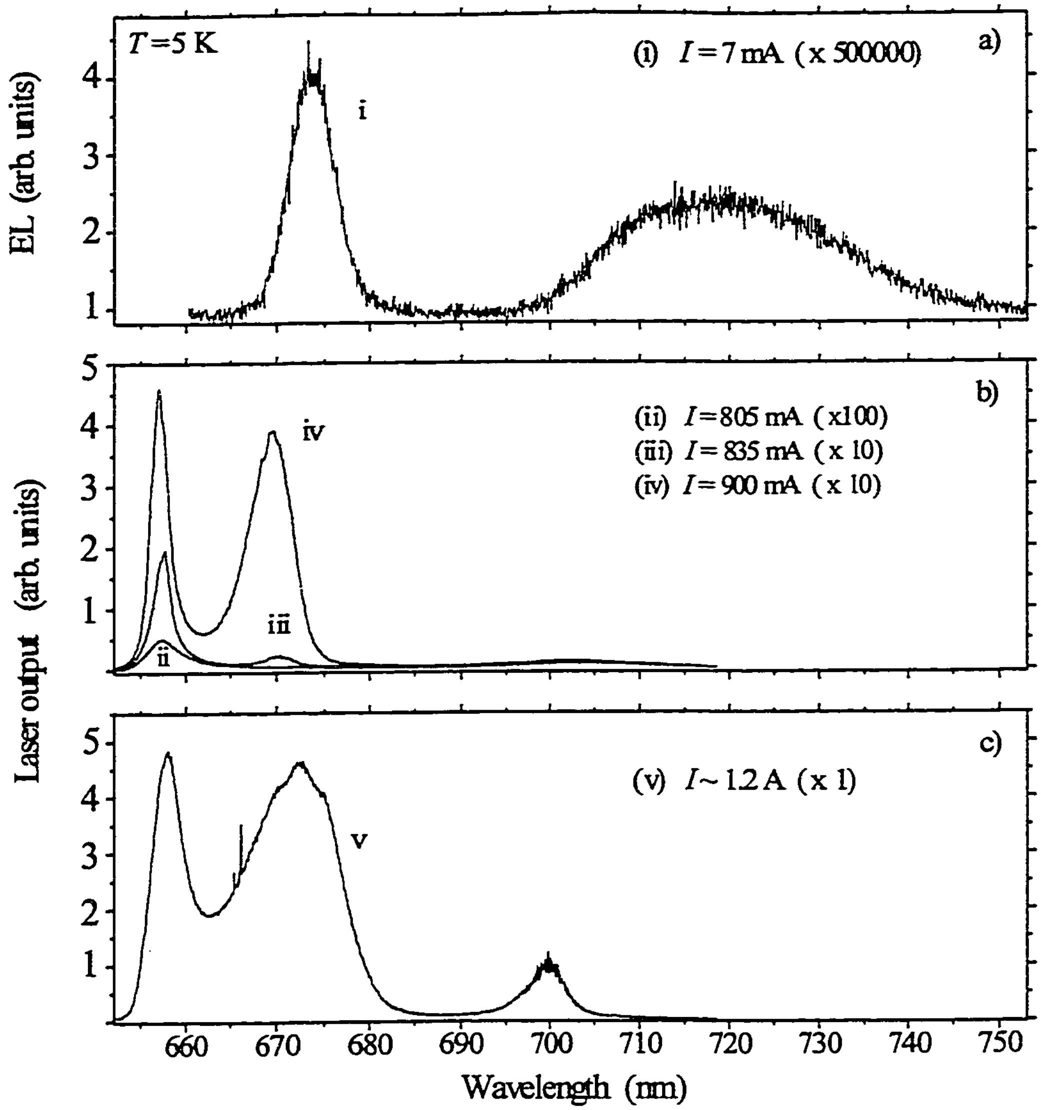

Figure 4.4 Spontaneous and stimulated emission spectra of a ~ 1 mm wide by ~ 1 mm long piece of sample *Ic* at 5 K. In (a), curve i displays spontaneous emission at very low currents from the WL and QDs. The spectrum noise is due to the very weak light emission at such a small pulsed injection current. In (b), curve ii demonstrates spontaneous emission from the $Al_{0.25}Ga_{0.75}As$ barriers which changes to stimulated emission in iii. As the current is increased above 900 mA, the wetting layer peak is also contributing to the lasing. For large currents (c) laser emission from the residual QDs is also observed (curve v). The broadness of the WL peak could be caused by monolayer fluctuations in the WL and/or many body effects such as bandgap renormalization and band filling.

length imposes a narrow mode spacing. This very thin QW is comparable to the WL in the QD sample (sample *Ia*); its EL spectra has only a small but identifiable QD contribution. This allows us to deduce that the stimulated emission observed in the QD sample originates from the QDs.

The observation of some residual QD emission in the very low current spontaneous emission spectra, and the high current stimulated emission spectra of sample *Ic* suggest that the 2-ML deposition corresponds to the early stages of island formation. The thin quantum well can therefore be expected to be sprinkled with low density islands having good uniformity [57, 73].

Sample *Ib* has a slightly thicker deposition of InAlAs (2.5 ML compared with 2 ML for *Ic*). At $T = 5$ K, for low current densities, the behavior of sample *Ib* is similar to that observed with the 4.5 ML laser structure (sample *Ia*): the spontaneous emission and stimulated emission originate from the QDs exclusively (figure 4.5a) with a lasing threshold of ~ 200 mA ($J_{th} = 830$ A/cm^2). We can therefore deduce that this sample has a higher island density than sample *Ic*.

However, as shown in figure 4.5b, when the current is increased to 1.5 A at $T = 5$ K, in addition to the QD lasing at $\lambda = 703$ nm ($h\nu = 1.764$ eV), weaker peaks originating from the bulk $Al_{0.25}Ga_{0.75}As$ and from the WL appear at $\lambda = 670$ and 658 nm ($h\nu = 1.851$ and 1.884 eV), respectively. Also, at 80 K sample *Ib* displays the QD, wetting layer, and the bulk $Al_{0.25}Ga_{0.75}As$ peaks for currents just below lasing threshold, as displayed in figure 4.6. For currents above lasing threshold, at 80 K the sample shows a behavior similar to that at 5 K. These radiative recombinations observed at higher temperatures or higher currents, or both, indicate that the injected carriers transit in the wetting layer and the bulk $Al_{0.25}Ga_{0.75}As$ of sample *Ib* for a relatively longer time than in those of sample *Ia*. The lasing properties obtained with samples *Ib* and *Ic* are therefore in contrast to the

Ia QD laser structure for which no bulk or wetting layer emission could be observed for any currents from 5 to 77 K. This result indicates that if the density of QDs is large enough, all the injected carriers are captured and thermalize efficiently to the QDs.

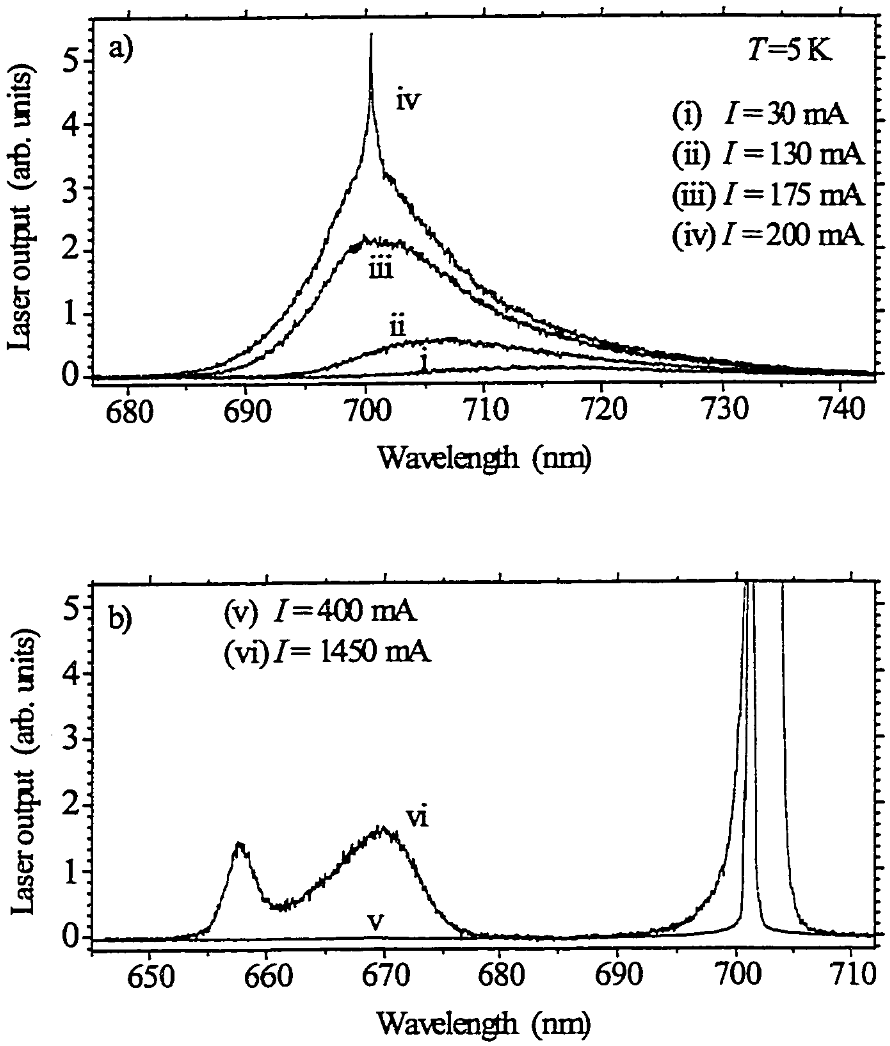

Figure 4.5 EL spectra of sample *Ib* at 5 K. In (a) spontaneous and stimulated emission from the QDs, the curves have a behavior comparable to sample *Ia* (figure 4.3a). For large currents (b) laser emission from the WL and $Al_{0.25}Ga_{0.75}As$ barrier is also observed.

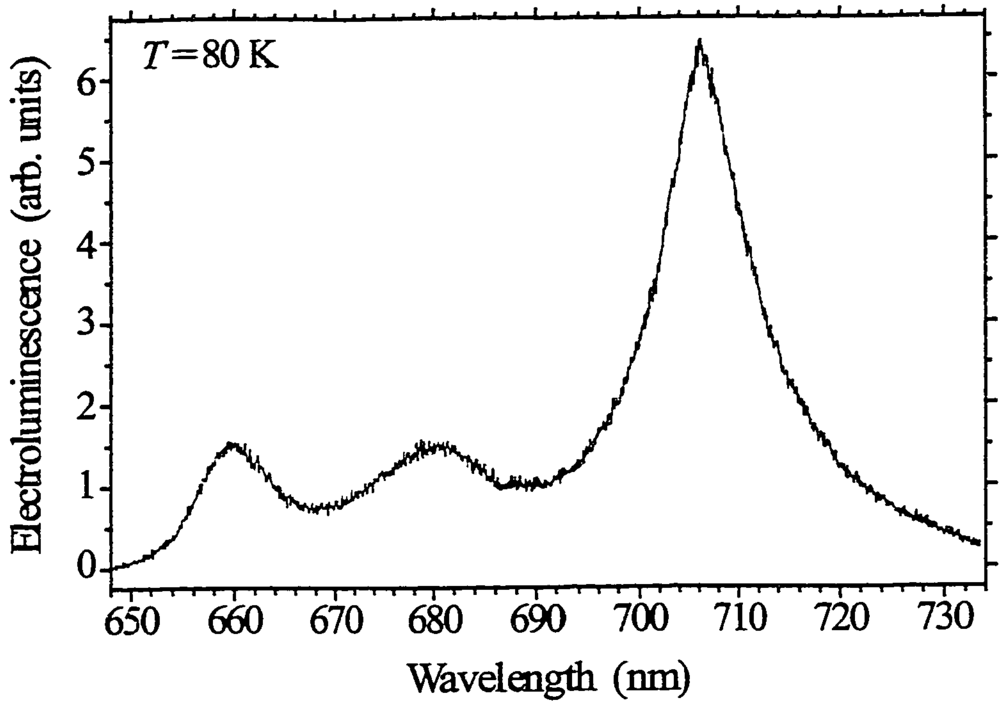

Figure 4.6 EL spectrum of sample *Ib* at 80 K just below lasing threshold (I = 550 mA). The QD peak centered at $\lambda = 706$ nm has a narrow spectral distribution characteristic for just below threshold conditions and changes to a stimulated peak at I =564 mA. The bulk $Al_{0.25}Ga_{0.75}As$ and WL peaks at $\lambda = 658$ nm and $\lambda = 678$ nm will only emit stimulated emission at very high current (850 mA).

4.2 Photoluminescence

PL measurements on the (110) surface of a small piece of sample *Ia* were done at 77 K. The incident laser beam was focussed on the cleaved face of the sample to a spot 50-100 μm diameter. Figure 4.7 displays the PL spectrum for an excitation power of 72 mW. The dominant peak at λ = 631 nm ($h\nu$ = 1.965 eV) corresponds to the $Al_{0.33}Ga_{0.67}As$ contact layer. This peak dominates the PL spectrum since the $Al_{0.33}Ga_{0.67}As$ material is the most abundant material in the structure. A shoulder at λ =

638 nm ($h\nu$ = 1.943 nm) matches the $Al_{0.30}Ga_{0.70}As$ cladding layer bandgap energy. The weak emission peak at λ = 668 nm ($h\nu$ = 1.856 eV) originates from the $Al_{0.25}Ga_{0.75}As$ barrier material. The double peak at lower energies (λ = 711 nm and 731 nm, $h\nu$ = 1.744 and 1.696 eV) is attributed to the QD emission from the ground state and excited states respectively. A 100 fold decrease in the pump intensity still produced state filling effects in the QD emission. However, a shift in the incident laser beam position away from the dots, resulting in the probing of the barrier materials mostly, revealed emission from the QD ground states only (λ = 736 nm). For this case, the $Al_{0.33}Ga_{0.67}As$ peak is 7 times more intense than the peak originating from the QDs. This procedure results in a much lower effective excitation intensity of the QD region, meaning that for this excitation level the QD's ground state does not saturate.

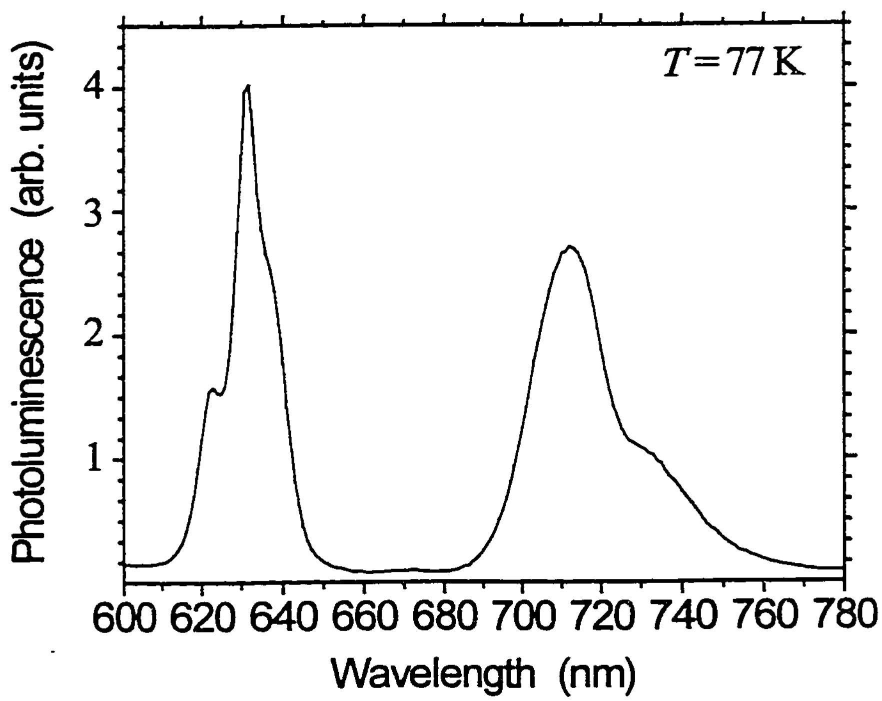

Figure 4.7 PL spectrum of sample *Ia* at 77 K with a high excitation intensity (72 mW).

4.3 Photovoltage

PV measurements were performed on samples *Ia* and *Ic* in order to obtain further information on their structural characteristics. The PV spectra in figure 4.8 confirm that sample *Ic* does not have many QDs: for sample *Ia*, a broad peak which is coincident with the EL/PL emission and attributed to the InAlAs QDs is seen at $\lambda \sim 710$ nm ($h\nu = 1.75$ eV), whereas sample *Ic* shows no peak at this wavelength. However, a shoulder located at $\lambda \sim 670$ nm ($h\nu = 1.85$ eV), which is consistent with both EL and PL results and assigned to the InAlAs WL, is observed. In both cases, a large peak is dominating the spectra at higher energies. For sample *Ia*, the $Al_{0.30}Ga_{0.70}As$ cladding layer seems to dominate the PV spectrum since the uppermost values are at wavelengths around 640 nm ($h\nu = 1.94$ eV), while for sample *Ic* it seems to be the $Al_{0.33}Ga_{0.67}As$ contact layer that dominates since the maximum intensities are around 622 nm ($h\nu = 1.99$ eV). Shoulders on both sides of the main peak in sample *Ia* can be attributed to the structure contact and buffer layers. In the spectrum for sample *Ic*, the two faint shoulders at energies lower than the main peak can be attributed to the cladding and buffer layers of the device.

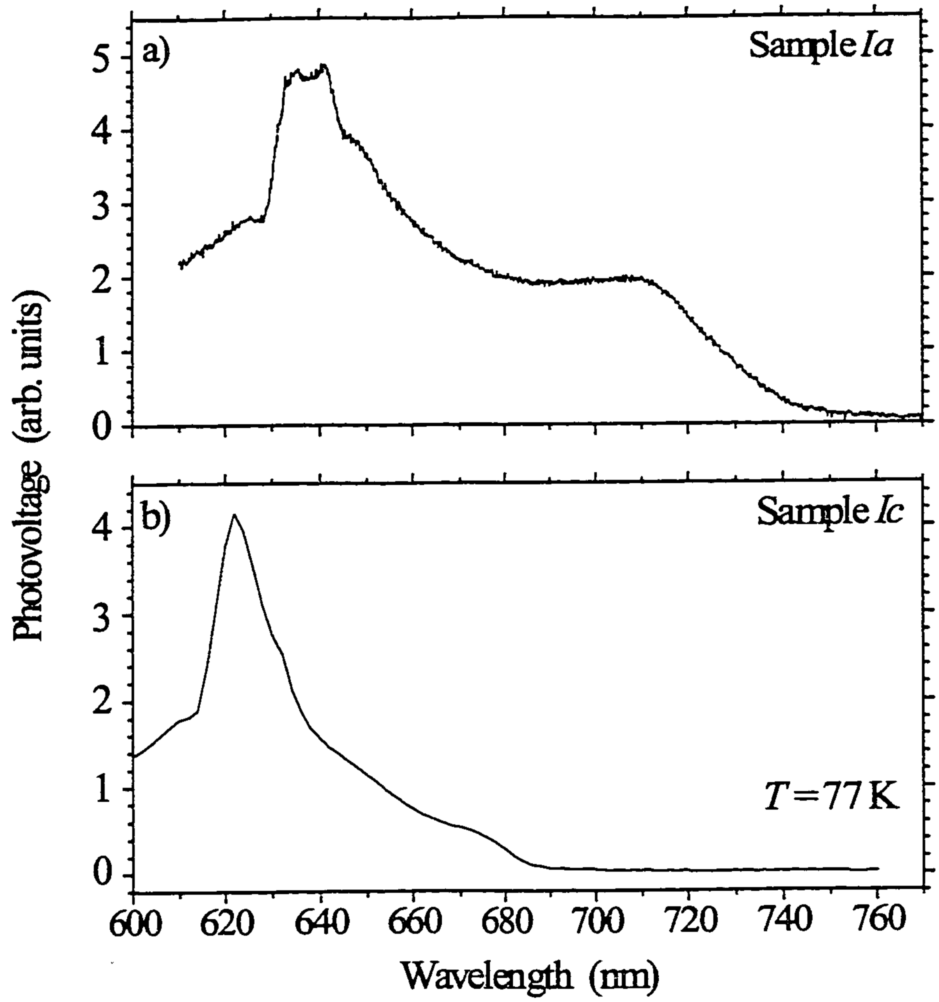

Figure 4.8 PV measurements at 77 K of (a) sample *Ia* and (b) sample *Ic*. In (a), the two main peaks are situated at $\lambda \sim 640$ and 710 nm. In (b), the two foremost peaks are located at $\lambda \sim 622$ and 670 nm.

4.4 Laser operating characteristics

The quantum efficiency of sample *Ia* at 5 K was investigated by monitoring the output power emitted (*L-I* characteristics) from one of the cleaved facets as a function of injected current for pulsed electrical excitation. Figure 4.9a shows the output power and figure 4.9b displays the external efficiency for injection currents up to 2 A. The threshold current density is 560 A/cm^2, and the differential efficiency above threshold is 0.2 mW/mA. The one-facet power output reached 200 mW at 1.9 A. From the current-voltage characteristics, a residual series resistance of 1.6 ohms is deduced, so, if correction for the power loss in this resistance is taken into account, the net external quantum efficiency (for both facets) is calculated at ~ 8.5%. This result indicates that the internal gain in the individual QDs is high compared with similar double-heterostructure QW and bulk lasers. The capture and thermalization of the injected carriers must be efficient, since the QD coverage is at most 50% and, due to the state distribution width of ~ 60 meV, only a small fraction (estimated to be 5%) of the QDs can emit at the lasing energy. Figure 4.10 displays the temperature dependence of the threshold current density for sample *Ia*. The threshold current density of the QD laser changed little between 5 and 77 K but increased quite rapidly above 80 K. This decrease in the QD laser efficiency at higher temperatures is most likely due to a nonoptimized design of the separate confinement which is discussed later in section 4.5.

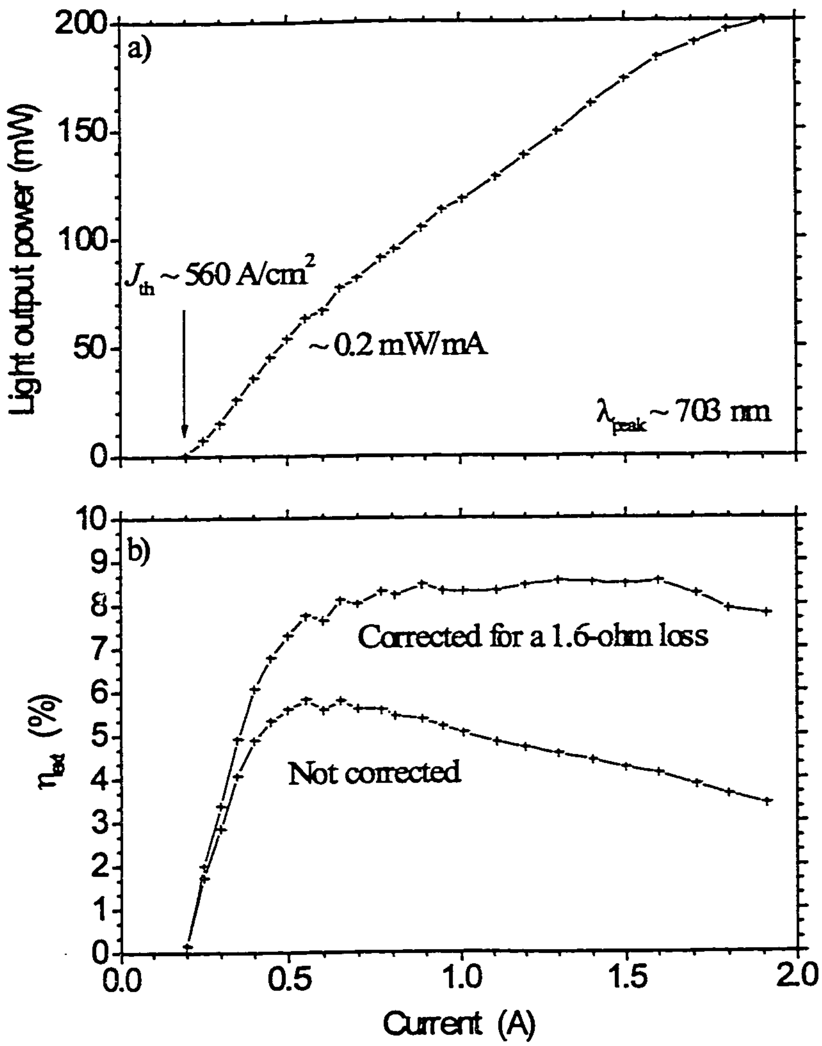

Figure 4.9 Lasing properties of sample *Ia* at 5 K as a function of the injection current for forward-bias pulses. (a) Peak power emitted from one facet; (b) two-facet electrical-to-optical conversion efficiency η_{eo} with and without corrections for the power losses in the residual 1.6-ohm contact resistance.

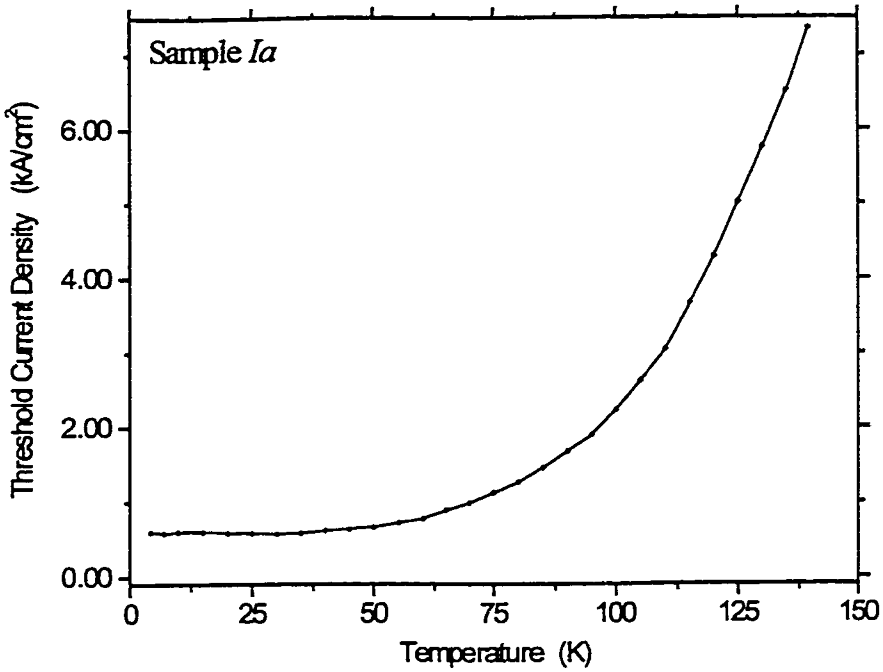

Figure 4.10 Temperature dependence of the threshold current density for sample *Ia*. Measurements where done on a 60-μm wide by 400-μm long laser cavity.

4.5 Effects of the confinement potential

To obtain room-temperature laser operation, sample *IIa* was grown with confining barriers higher than those of sample *Ia* (refer to figure 3.2). Sample *IIa* has 5.0 ML of $In_{0.64}Al_{0.36}As$ nominally deposited while sample *Ia* had only 4.5 ML, this should result in a higher dot density and a larger inhomogeneous broadening of the spontaneous emission linewidth.

4.5.1 Electroluminescence

The $T = 5$ K emission from sample *IIa* is displayed in figure 4.11. Unlike what was observed for sample *Ia*, no Gaussian lineshape is observed at low injection currents; instead an asymmetric peak shifted toward higher energies is seen indicating that state filling effects are present in this structure as well. The lineshape depicted in figure 4.11a was also observed at $T = 77$ K with the same laser, as well as with other laser devices processed from the same wafer at the same temperatures. With increasing current, a stimulated emission peak at $\lambda = 686$ nm ($h\nu = 1.807$ eV) appears on top of the spontaneous asymmetric peak. Compared to the earlier samples, the peak position is shifted towards higher energies, which could be the result of a smaller average dot size, a different dot alloy composition, a different growth temperature for this sample, emission from higher QD excited states as compared to sample *Ia*, or a combination of these effects.

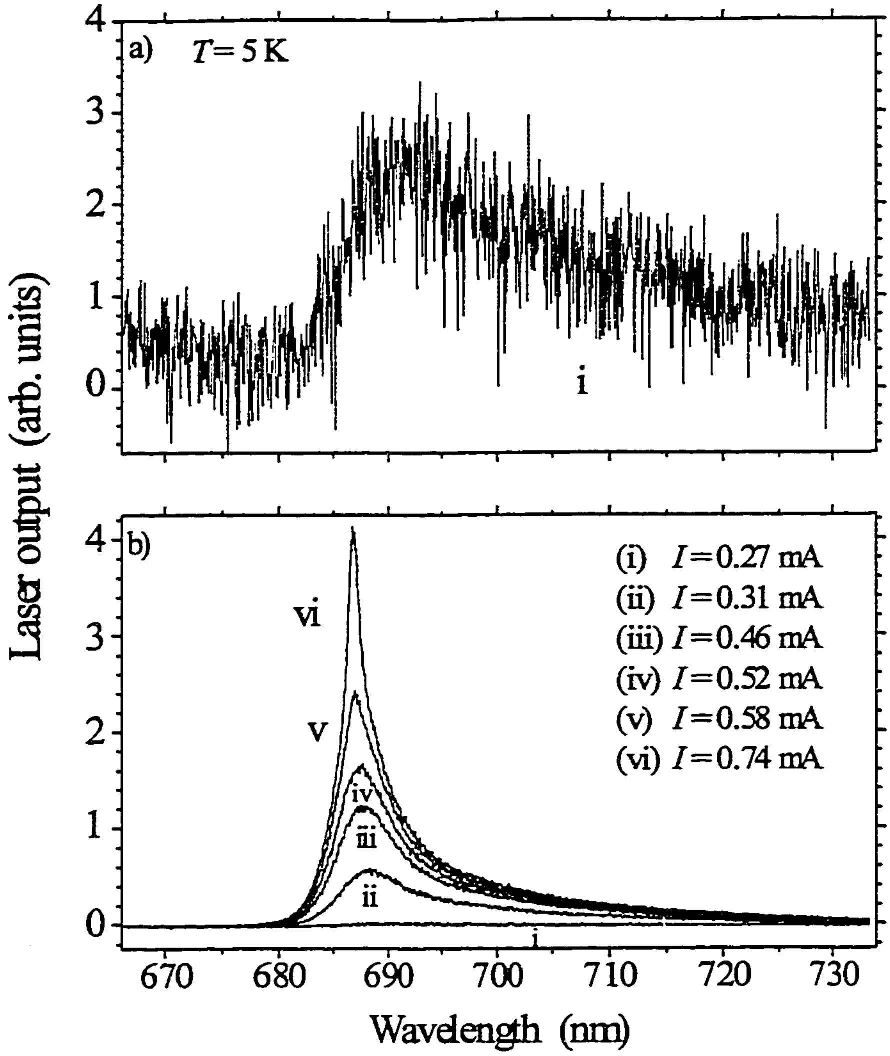

Figure 4.11 Spectral output at 5 K of sample IIa. In (a), the data is for a current density of 1.7 A/cm^2 and represents a blow-up of the bottommost curve seen in (b). The noise in the spectrum is due to the very weak light emission at such a small pulsed injection current. In (b) the current densities varies from 1.7 A/cm^2 for the lowest curve to 4.6 A/cm^2 for the top curve.

As the sample temperature is increased from 50 to 140 K, the laser emission energy shifts gradually from excited states emission to ground states of the QDs, as shown in figure 4.12. The shift is gradual due to the varied inter-sublevel energy spacings included in the QD ensemble. The room temperature spectral output of sample

IIa is displayed in figure 4.13. Curve (i) shows the spontaneous emission from the QDs ground states; its Gaussian lineshape reflects the inhomogeneous broadening of the QD ensemble. Curve (ii) is taken slightly above threshold at 4.4 kA/cm^2, and shows at 723 nm ($h\nu$ = 1.75 eV) room-temperature stimulated emission.

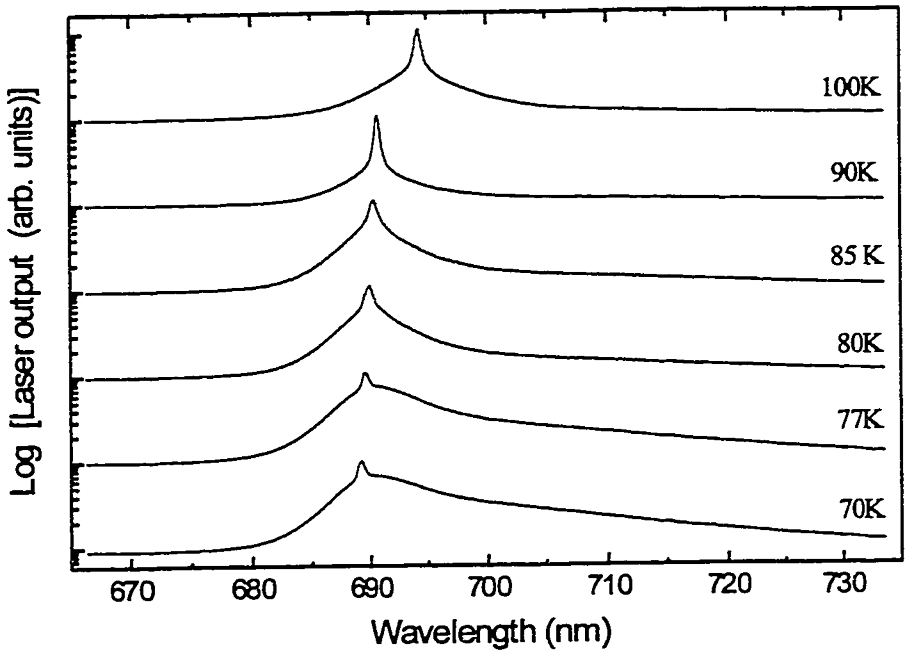

Figure 4.12 Sample *IIa* threshold stimulated emission of a 40 μm x 400 μm cavity for temperatures between 70 and 100 K. As the temperature is increased, a shift in the spontaneous emission line shape from asymmetric towards symmetric is observed. The stimulated emission peak position also shifts in the same manner.

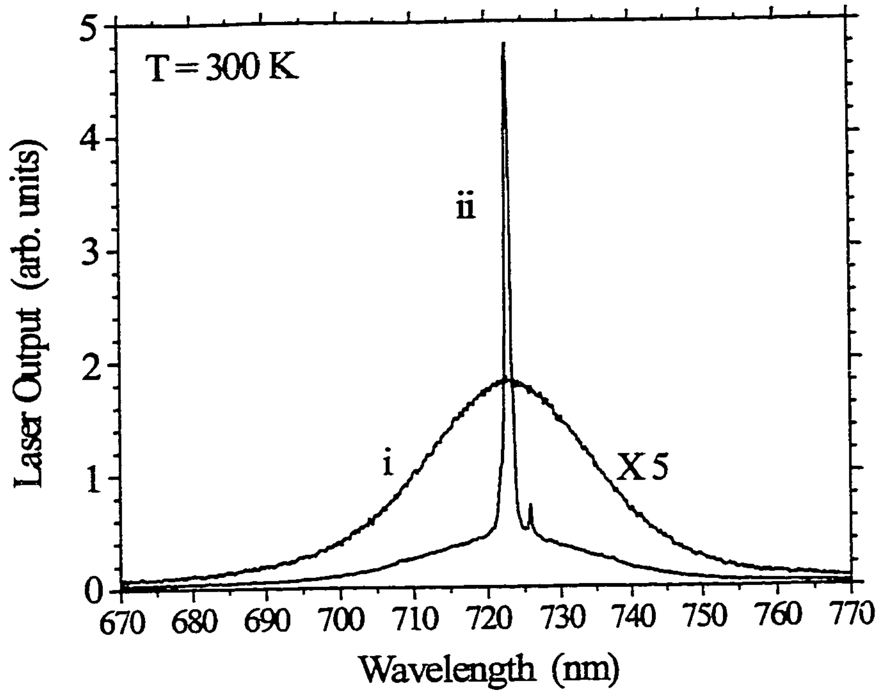

Figure 4.13 Room temperature spectral output of sample *IIa* before and after threshold: for $J = 4.0$ kA/cm^2 (i); and $J = 4.4$ kA/cm^2 (ii).

The fact that the EL spectra at low temperatures and low currents displays state filling, indicates impeded carrier thermalization and radiative recombination from the excited states. This means that the inter-sublevel and interband relaxation dynamics are comparable for this sample at very low carrier density and at low temperature. As the temperature is increased, the emission shifts towards lower energies. This behavior reflects the increased thermionic emission rates of the carriers in the higher-energy excited states, and the larger phonon population which can help carrier thermalization to the ground states. These effects are displayed in figure 4.14. Efficient carrier relaxation to lower states occurs predominantly by longitudinal acoustic phonon emission if the energy levels are separated by no more than a few meV, or by longitudinal optic phonon emission if the levels are within a few tens of meV from each other [37, 74, 75]. The accepted value for the InAs-like longitudinal-optical phonon energy is 30 meV and for the AlAs-like longitudinal-acoustic phonon it is 50 meV [63]. Sample *Ia*'s energy level spacing could be close to one of these values; this might not be so for sample *IIb*. These two samples probably have different energy level spacings due to their different InAlAs deposited amounts as well as their different potential barrier heights.

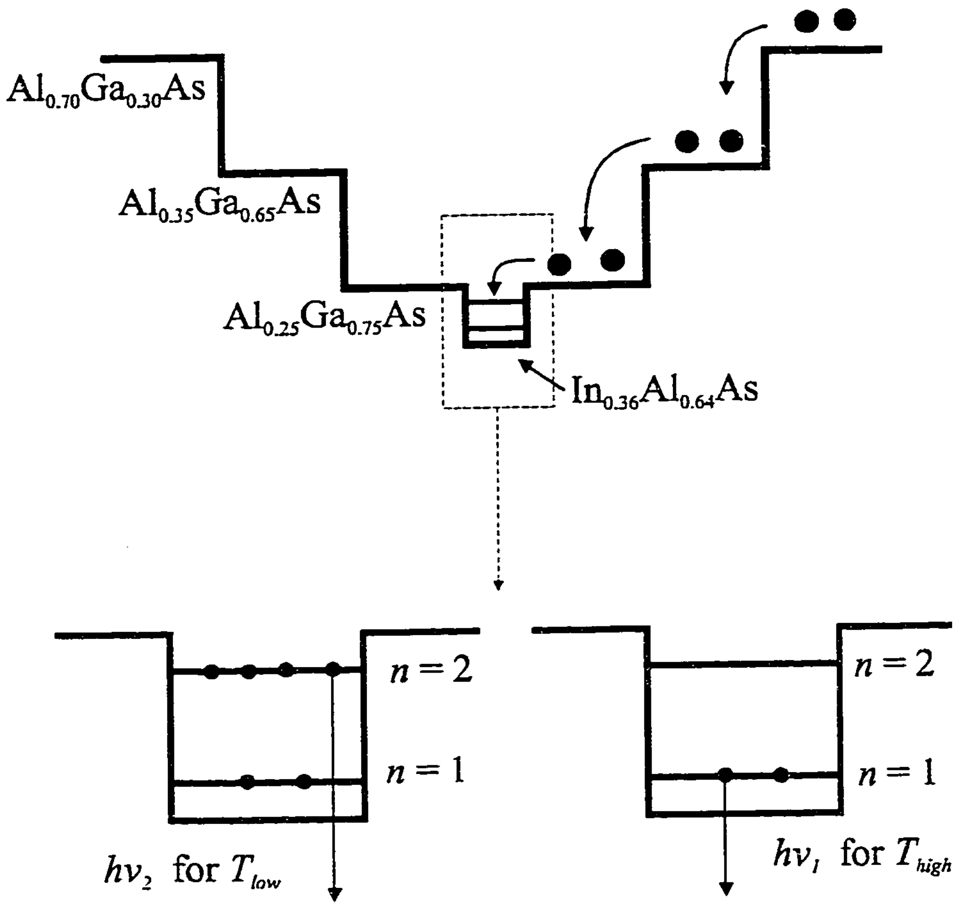

Figure 4.14 Sketch of the temperature effect in one specific QD. For temperatures T_{low}, the state filling effect is present due to a small phonon population impeding carrier thermalization to the ground state and a low thermionic emission rate of the carriers over the barrier permitting recombination to take place in the excited states. For temperatures T_{high}, a large amount of phonons is available to assist in thermalization of the carriers to the ground state.

4.5.2 QD and control QW laser characteristics

Figure 4.15 compares the temperature dependence of the threshold current density (J_{th}) for samples *Ia* and *IIa*. For temperatures below 50 K in sample *Ia*, the lasing threshold is almost independent of temperature, but for higher temperatures the threshold increases rapidly and can be explained by the shallow separate confinement structure. This is further confirmed by comparing these results with the ones obtained from sample *IIa*; in this case, the temperature range for which the threshold has little temperature dependence extends to $T \sim 75$ K. Another effect of the higher confining barriers is the sharp decrease in the threshold current density at low temperatures from J_{th} around 650 A/cm^2 in sample *Ia* to record low values of ~ 2 A/cm^2 in sample *IIa*.

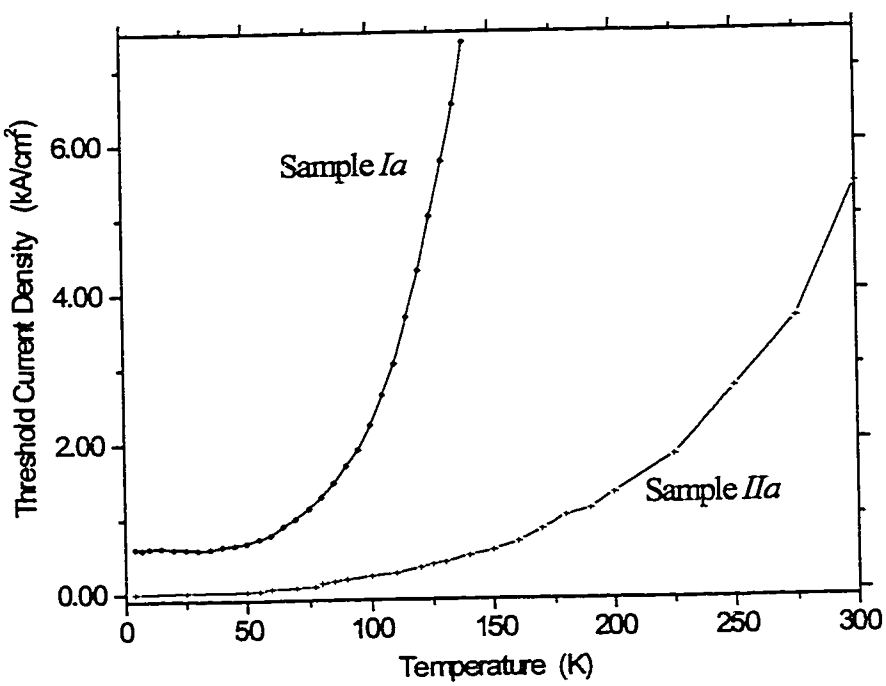

Figure 4.15 Temperature dependence of the threshold current density for samples *Ia* and *IIa*.

A control laser diode structure was grown with 5 QWs instead of one QD layer to observe possible advantages of these zero-dimensional devices over two-dimensional ones. This structure was grown using the same sequence as before but with active regions incorporating QWs instead of QDs by using thinner $In_{0.64}Al_{0.36}As$ layers, thus stopping the growth prior to the island formation. TEM results show 1-2 nm thick QWs with no QD formation and, at $T = 5$ K, the Fabry-Perot laser cavity emits at $\lambda = 682$ nm ($h\nu = 1.818$ eV). Figure 4.16 shows the temperature dependence of the threshold current density for this thin multiple QW sample and for sample *IIa*. At temperatures below 125 K, the thresholds of the InAlAs QW laser have a slightly more pronounced temperature dependence than the ones of sample *IIa*. At higher temperatures however, the thresholds of the QW and QD lasers are somewhat comparable, allowing for room temperature operation at a few kA/cm^2. This suggests that at higher temperatures, when the thermionic emission rates of the injected carriers out of the QD or QW potential become important, the lasing threshold is governed by the depth of the separated confinement region relative to the laser emission energy, with little dependence on the dimensionality of the potential.

A 5.0 nm-thick GaAs/AlGaAs quantum well laser with the same confinement structure as sample *IIa* (sample *III*) was studied to confirm these results. Indeed, the lasing threshold of such a standard QW structure clearly displays a continuous temperature dependence similar to the one found with the InAlAs control QW laser. In the case of sample *III* however, the overall temperature dependence is weaker because the 5.0 nm GaAs QW laser emits at a lower energy of ~ 1.59 eV (emission in the infrared at $\lambda \sim 780$ nm, an energy ~ 200 meV lower than for sample *IIa*). Therefore, for sample *III*, the potential of the GaAs QW being deeper with respect to the $Al_{0.25}Ga_{0.75}As$ barrier will reduce the thermionic emission rates of the injected carriers, resulting in lower thresholds. It can be expected that QD lasers emitting at longer wavelengths would behave similarly. Infrared QD lasers having the same barrier materials as sample *IIa* will have a significantly larger potential difference between the QD energy levels and the barrier bandgap energy. Thus, compared with sample *IIa*, infrared QD lasers should display a distinct reduction in the threshold currents, and should have improved characteristics when operating at room temperature.

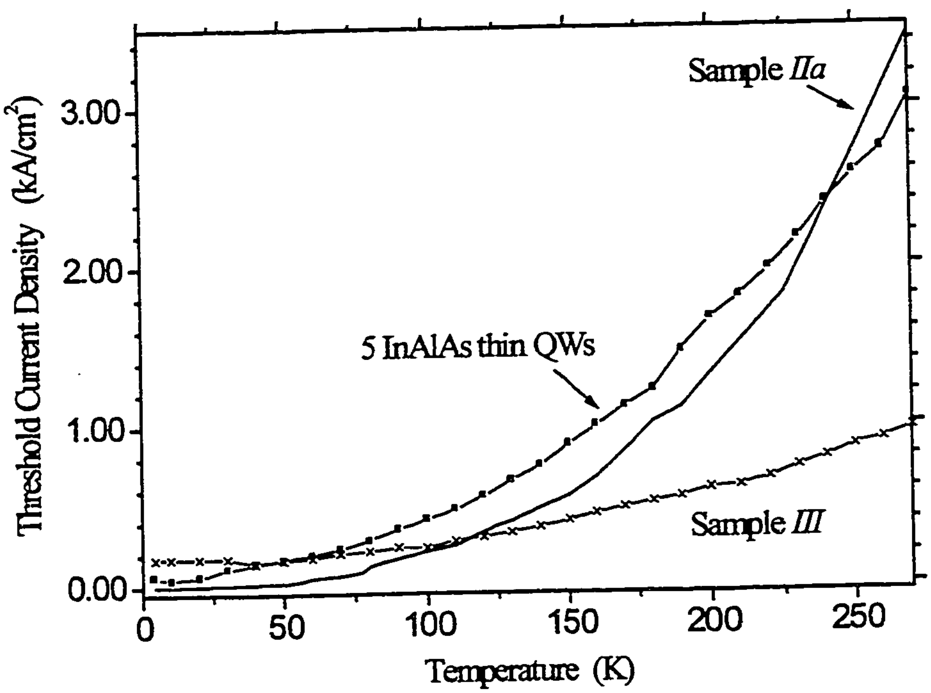

Figure 4.16 Temperature dependence of the threshold current density for various lasers with $Al_{0.70}Ga_{0.30}As/Al_{0.35}Ga_{0.65}As/Al_{0.25}Ga_{0.75}As$ separate confinement layers. Sample *IIa* and *III* are 40 μm x 400 μm laser cavities, the thin InAlAs QW has a 60 μm x 400 μm laser cavity.

The results above can be compared with the theoretical models described by Arakawa and Sakaki [4] and Asryan and Suris [51]. For temperatures below ~ 50 K, the threshold current density of sample *IIa* increases very slightly as a function of temperature. Therefore the systems behavior is close to that of an ideal QD system (figure 2.7d), and the inhomogeneous broadening of the QD ensemble does not affect J_{th}. At higher temperatures, the finite potential barriers causes equilibrium filling of the QDs, producing a steady increase in the QD laser threshold current density as a function of temperature. The models are not well suited for a quantitative comparison with experiment, since they only take ground-state stimulated emission into account, without considering the possible effects resulting from excited state stimulated emission such as larger degeneracy in the higher-order QD electron states.

The efficiencies of the broad area lasers from sample *IIa*, that is the single-layer improved-confinement QD laser, and from the control GaAs QW laser, sample *III*, have been investigated in the temperature range where the threshold has a weak temperature dependence. Figure 4.17 shows the external efficiency for injection currents up to 0.5 A. The threshold current for sample *IIa* is 335 A/cm^2 in continuous wave operation mode and the differential efficiency above threshold is ~ 0.2 mW/mA. The net external quantum efficiency (for both facets) is ~ 13 %. This value can be compared with the curve for sample *III*. In the case shown in figure 4.17, the QD laser efficiency slightly exceeds the QW efficiency, and generally for the QD samples studied, the external efficiency values vary between 5 and 13 %. Clearly the external efficiencies obtained with the QD lasers are comparable with the one obtained with a standard QW laser.

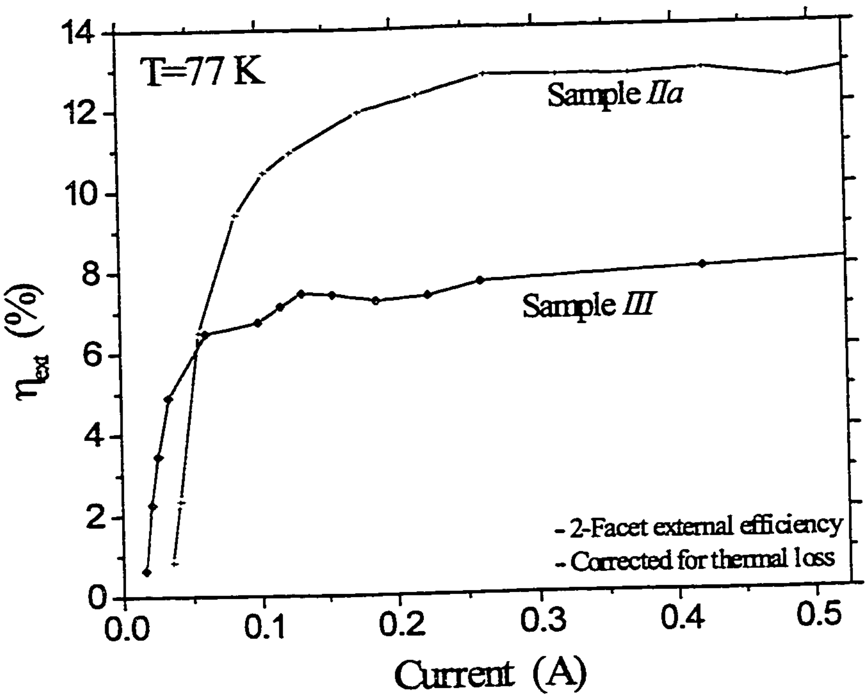

Figure 4.17 Comparison between the external electrical to optical efficiency measured with samples *IIa* and *III* at 77 K.

The effects of the QD surface density on the laser structure characteristics were studied with the help of a sample having the same configuration and growth conditions as sample *IIa*, but with only 4.5 ML of InAlAs material deposited. The TEM revealed a low dot density of 17 ± 8 dots/μm^2 compared to sample *IIa* with 500 ± 200 dots/μm^2 and a dot base width of ~ 20 nm like in sample *IIa*, so that the 4.5 ML laser has ~ 0.4 x 10^6 dots under a 60 μm by 400 μm gate whereas sample *IIa* has ~ 12 x 10^6 dots. The two samples have similar threshold curves. At the lasing threshold, the line width is only 2-3-meV wide for sample *IIa* and the 4.5-ML sample (figure 4.13), so that only a small subset of the QD ensemble contributes to the optical gain. Sample *IIa* should have wider inhomogeneous broadening than the 4.5 ML sample since larger dot densities in a QD layer is indicative of larger inhomogeneous broadening [57, 59]. Therefore, at the lasing threshold, sample *IIa* utilizes a narrower portion of the total dot energies available than the 4.5 ML QD laser, explaining the similar threshold curves between the two QD lasers. As the current density is increased, the FWHM of the stimulated emission broadens to ~ 6 meV with $J = 1.8$ kA/cm^2 for the 4.5 ML QD laser and to ~ 8 meV with $J = 2.0$ kA/cm^2 for sample *IIa*. The lower dot density does not affect the laser characteristics significantly: the temperature dependence of the threshold current density is slightly higher for the 4.5 ML QD laser than the ones for sample *IIa*. Both lasers exhibit equivalent behaviors indicating little dependence of the threshold on the dot density.

4.6 Multi-layer QD structures

According to the waveguiding simulations done in section 2.5.2, the confinement factor should increase significantly if the number of QD layers in the active region is increased. Sample *IIb* has the same separate confinement structure as *IIa* but the active region is wider with five layers of dots sandwiched between 8 nm $Al_{0.25}Ga_{0.75}As$ spacer layers. The TEM of sample *IIb*, shown in figure 3.3c, displays a clear increase in the dot sizes in the upper layers, suggesting an increased inhomogeneous broadening of the QD ensemble's state distribution. At low temperatures and low currents, the laser structure from this sample behaves similarly to sample *Ia*; at very low currents, a symmetric peak centered at $\lambda = 750$ nm ($h\nu = 1.653$ eV) is observed which shifts towards high energies as the injection current is increased. The symmetric peak has a FWHM = 157 meV: three times wider than what was measured for sample *Ia*. At high currents, emission from the

WL is also observed; for temperatures around 77 K and above, WL lasing does not occur. At $T = 77$ K the threshold stimulated emission is still from excited states at ~ 710 nm ($h\nu$ = 1.746 eV), and as the current is increased, the stimulated emission linewidth broadens significantly. As displayed in figure 4.18, at a current density of 3.0 kA/cm^2 the FWHM of the lasing line is 35 meV (14.5 nm). This value is much larger than any observed with either single QD layer samples for high current densities diodes (for sample *IIa* at $J = 2.0$ kA/cm^2, the FWHM was ~ 8 meV), or for QW broad area laser (for sample *III* at $J = 1.7$ kA/cm^2, the FWHM was ~ 4 meV). The larger inhomogeneous broadening of the QD ensemble allows for a larger gain bandwidth in the stimulated emission process.

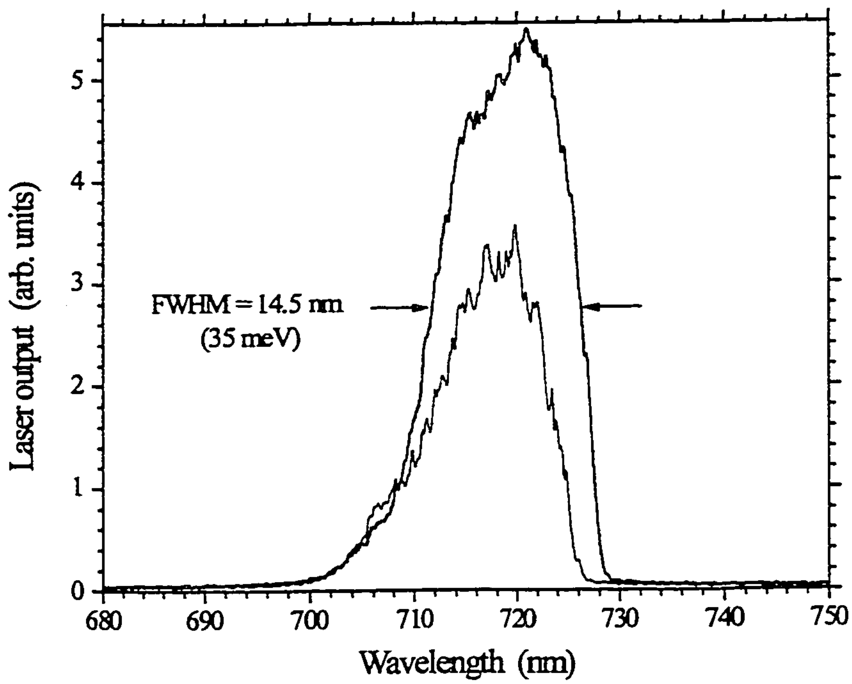

Figure 4.18 Laser output at $T = 77$ K of sample *IIb* in a 60 μm x 400 μm cavity. The bottom curve is for an injection current of 450 mA. The top curve is for a current of 720 mA, and the laser line has a FWHM of 35 meV.

Figure 4.19 displays the temperature dependence of the threshold current density for sample *IIb*. The curve has a shape equivalent to that of sample *IIa*, but the values are

~ 1 kA/cm^2 above the ones for the single layer QD sample. Here, the increase in the number of dots from sample *IIa* to *IIb* does not lower the threshold current density. In this case, this might in part be caused by the diffusion of the beryllium doping across the active region (which was observed by SIMS for this sample), and also by the larger inhomogeneous broadening of the QD ensemble.

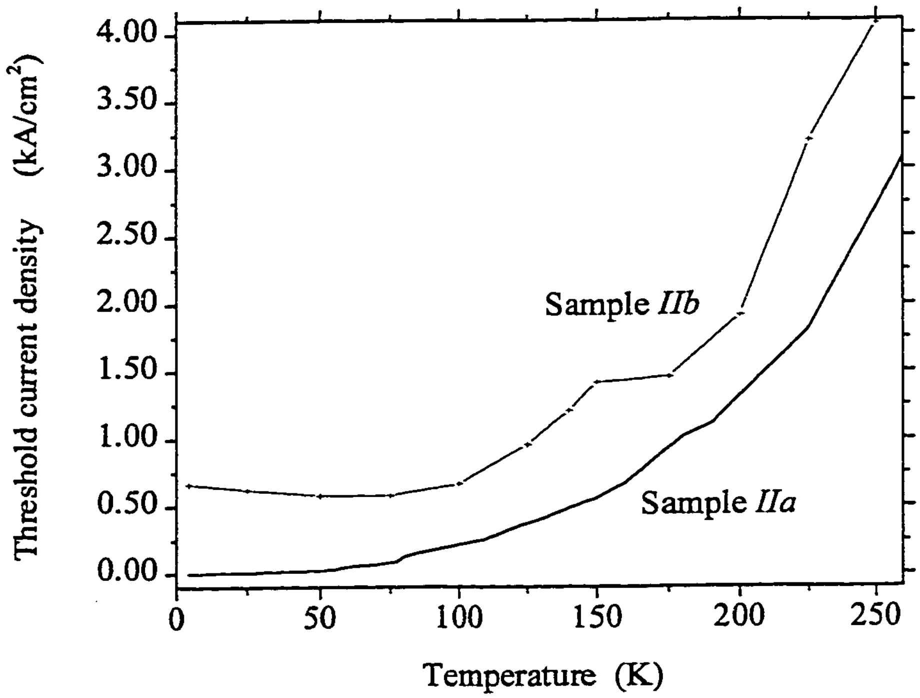

Figure 4.19 Temperature dependence of the threshold current density for samples *IIa* and *IIb*.

A wafer with the same structure as sample *IIb* was grown but with 50 nm $Al_{0.25}Ga_{0.75}As$ spacer layers instead of 8 nm. The TEM results show that the first layer has a large dot density, but that the subsequent ones have very low densities. No vertical self-assembling is observed since the strain fields induced by the dots do not propagate through such wide spacer layers, and the QD dimensions are similar to the ones from sample *Ia*. The spontaneous emission spectra at low injection currents show a small FWHM of the inhomogeneous broadening. However, because the active region is quite wide (300 nm thick), the device characteristics are worse than the ones of sample *IIa*. Also at low current, the WL dominates the stimulated emission due to the small amounts of dots present. Therefore the gain in the QDs can be increased by reducing the dot layer spacing, and the emission linewidth can be kept narrow by assuring that the growth is not correlated from layer to layer.

Chapter 5

CONCLUSIONS

In this study, the results from the investigation of several QD lasers in the strained InAlAs/AlGaAs system were presented. Stimulated emission originating from the QDs was clearly demonstrated. For samples with small QD densities, emission from the WL was also observed. Other research groups have now investigated laser radiation from self-assembled quantum dots in different material systems: InGaAs QDs imbedded in a GaAs heterostructure [72, 76-79], InAs dots in a GaAs matrix [80, 81] and InGaAlAs/GaAs QDs [82]. All these quantum dot lasers emit in the infrared between 950 nm and 1300 nm. In this work, the dots studied emit in the 700-nm region of the electromagnetic spectrum; this pushes quantum dot laser emission into the visible. In the near future, different material systems such as GaN will lead to even shorter wavelength QD lasers.

For the QD sample with the lower potential barriers, state filling effects are seen, and lasing occurs via excited state emission. For the single layer QD laser with improved confining layers, stimulated emission at low temperatures originates from excited states recombination indicating impeded carrier thermalization and radiative recombination. As the temperature increases, increased phonon population and thermionic emission of the carriers in the higher excited states contributes to shift the emission to ground-state energies.

Other studies of QD and quantum wire laser systems [83], report stimulated emission originating from higher-order sublevels/subbands. It is shown by H. Shoji et al, that in the InGaAs/GaAs system, ground state emission is possible by increasing the number of QD layers and the cavity length to decrease cavity losses [84].

At low temperatures, the lasing threshold currents measured with the QD lasers are slightly more temperature-independent than the ones measured with control QW lasers. Also, the external efficiencies found with the QDs are comparable to, and even in some cases surpass, the ones measured on a standard GaAs QW. This supports the models presented by Arakawa and Sakaki, and Asryan and Suris. At higher temperatures, the temperature dependence of the threshold currents is governed mainly by the confining potentials at the emission energy, and by the depth of the separate confinement region. Short wavelength QD lasers capable of room temperature emissions with simple broad area laser devices having threshold current densities of a few kA/cm^2 can be readily produced. QD lasers that will be produced to operate at longer wavelengths (for example at 1.3-1.5 μm [21]) should therefore have lower thresholds.

Continuous wave operation at 77 K is achieved with a single layer higher carrier-confinement QD laser at current densities below 85 A/cm^2, with peak powers greater than 200 mW under high current injection. These results are very encouraging for device applications based on zero-dimensional structures.

Broad lasing linewidth (35 meV) is demonstrated in the five correlated-growth QD layer sample. Through the use of a new technique during growth, the inhomogeneous broadening of the QD ensemble has been diminished [85], even for closely spaced layers with vertical self-assembling. This method can be used to improve the gain of QD lasers by limiting the range of wavelengths that compete in the stimulated emission process.

The next step that should be undertaken to test the validity of QDs as active devices would be direct gain measurements in the InAlAs/AlGaAs system. This will allow a direct comparison of the gain coefficients between QD and QW laser structures. A system with higher confining barriers will significantly reduce the effects of thermionic emission permitting a better three-dimensional confinement up to room temperature. An example of such system is InAs QDs in a GaAs matrix. The emission from the different energy levels in the InAs/GaAs QD system give distinct peaks in PL and EL spectra. Consequently, this system is better suited for studying the carrier dynamics in the various energy levels. Measurements of carrier lifetimes in the different energy levels will help understand the basic processes taking place in these artificial atoms.

References

[1] L. Esaki and R. Tsu. Superlattice and negative differential conductivity in semiconductors, IBM J. Res. Develop. **14**, 61 (1970).

[2] C. Weisbuch and B. Vinter. "Quantum Semiconductor Stuctures". Academic Press, San Diego, pp. 19-21 (1991).

[3] R. Steele. Review and forecast of laser markets: 1997-Part II. Laser Focus World, February, 85 (1997)

[4] Y. Arakawa and H. Sakaki, Multidimensional quantum well laser and temperature dependence of its threshold current, Appl. Phys. Lett. **40**, 939 (1982).

[5] Y. Arakawa, and A. Yariv. Quantum well lasers – gain, spectra, dynamics, IEEE J. Quantum Electron. **QE-22**, 1887 (1986).

[6] H. Sakaki. Quantum wires, quantum boxes and related structures: physics, device potentials and structural requirements, Surf. Science **267**, 623 (1992).

[7] M. Asada, Y. Miyamoto, and Y. Suematsu. Gain and the threshold of three-dimensional quantum-box lasers, IEEE J. Quantum Electron. **QE-22**, 1915 (1986).

[8] Y. Miyamoto, M. Cao, Y. Shingai, K. Furuya, Y. Suematsue, K.G. Ravikumar, S. Arai. Light emission from quantum-box structure by current injection, J. Appl. Phys. **26**, L225 (1987).

[9] S. Fafard, R. Leon, D. Leonard, J.L. Merz and P.M. Petroff, Visible photoluminescence from N-dot ensembles and the linewidth of ultrasmall $Al_yIn_{1-y}As/Al_xGa_{1-x}As$ quantum dots, Phys. Rev. B **50**, 8086 (1994).

[10] K. Kash. J. Lumin. **46**, 69 (1990).

[11] P.D. Wang, C.M. Sotomayor Torres, H. Benisty, C. Weisbuch, S.P. Beaumont. Radiative recombination in GaAs-$Al_xGa_{1-x}As$ quantum dots, Appl. Phys. Lett. **61**, 946 (1992).

[12] C.M. Sotomayor Torres, W.E. Leicth, D. Lootens, P.D. Wang, G.M. Williams, S. Thoms, H. Wallace, P. Van Daele, A.G. Cullis, C.R. Stanley, P. Demeester and S.P. Beaumont. Wires and dots in GaAs-GaAlAs quantum wells: luminescence intensity studies, *in* "Nanostructures and Mesoscopic Systems" (W.P. Kirk and M.A. Reed, eds) Academic Press, San Diego (1992).

[13] D. Heitmann and J.P. Kotthaus. The spectroscopy of quantum dot arrays, Physics Today **46**, #6 56 (1993).

[14] F. Daiminger, A. Schmidt, K. Peiger, F. Faller, and A. Forchel. Thermalization and band renormalization in the zero-dimensional electron-hole system in InGaAs/GaAs quantum dots, Semicond. Sci. Technol. **9**, 896 (1994).

[15] K. Brunner, U. Bockelmann, G. Abstreiter, M. Walther, G. Böhn, G. Tränkle, and G. Weimann, Photoluminescence from a single GaAs/AlGaAs quantum dot, Phys. Rev. Lett. **69**, 3216 (1992).

[16] O. Klein, C. de C. Chamon, D. Tang, D.M. Abush-Magder, U. Meirav, X.-G. Wen, M.A. Kastner, and S.J. Wind. Exchange effects in an artificial atom at high magnetic fields, Phys. Rev. Lett. **74**, 785 (1995).

[17] R. Leonelli, C.A. Tran, J.L. Brebner, J.T. Graham, R. Tabti, R.A. Masut, and S. Charbonneau. Optical and structural properties of metalorganic-vapor-phase-epitaxy-grown InAs quantum wells and quantum dots in InP, Phys Rev B **48**, 11135 (1993).

[18] C. Weisbuch and B. Vinter. "Quantum Semiconductor Structures", Academic Press, San Diego, pp. 191-197 (1991).

[19] U. Woggon. "Optical Properties of Semiconductor Quantum Dots", Springer, Berlin Heidelberg, Chap. 2 (1997).

[20] J.Y. Marzin, J.M. Gerard, A. Israel, D. Barrier, and G. Bastard. Photoluminescence of single InAs quantum dots obtained by self-organized growth on GaAs, Phys. Rev. Lett. **73**, 716 (1994).

[21] S. Fafard, Z. Wasilewski, J. McCaffrey, S. Raymond, and S. Charbonneau, InAs self-assembled quantum dots on InP by molecular beam epitaxy, Appl. Phys. Lett. **68**, 991 (1996).

[22] H.-C. Ko, D.-C. Park, Y. Kawakami, S. Fujita and S. Fugita. Self-organized CdSe quantum dots onto cleaved GaAs (110) originating from Stranski-Krastanow growth mode, Appl. Phys. Lett. **70**, 3278 (1997).

[23] D.J. Eaglesham and M. Cerullo. Dislocation-free Stranski-Krastanow growth of Ge on Si (100), Phys. Rev. Lett. **64**, 1943 (1990).

[24] S.-Z. Chang, T.-C. Chang, S.-C. Li. The growth of highly mismatched $In_xGa_{1-x}As$ ($0.28 \leq z \leq 1$) on GaAs by molecular-beam epitaxy. J. Appl. Phys. **73**, 4916 (1993).

[25] S. Fafard et al. *Unpublished.*

[26] F.C. Frank and J.H. van der Merwe. One-dimensional dislocations. I. Static theory, Proc. R. Soc. London A **198**, 205 (1949).

[27] I.N. Stranski and L. Krastanow. Zur Theorie der orientierten Ausscheidung von Ionenkristallen aufeinander, Akad. Wiss. Wien Ber. Math. Naturwiss. Kl. **146**, 797 (1937).

[28] M. Volmer and A. Weber. Keimbildung in übersättigten Gebilden, Z. Phys. Chem. **119**, 277 (1926).

[29] I.V. Markov. "Crystal growth for beginners, fundamentals of nucleation, crystal growth and epitaxy", World Scientific, Singapore, chap. 4 (1995).

[30] S. Raymond, S. Fafard, S. Charbonneau, R. Leon, D. Loenard, P.M. Petroff, J.L. Merz. Photocarrier recombination in $Al_yIn_{1-y}As/Al_xGa_{1-x}As$ self-assembled quantum dots. Phys. Rev. B **52**, 17238 (1995).

[31] S. Raymond, S. Fafard, and S. Charbonneau. Temperature dependence of ultra-sharp luminescence lines in AlInAs/AlGaAs self-assembled quantum dots, Can. J. Phys. **74**, s216 (1996).

[32] S. Fafard, S. Raymond, P.J. Poole, Y. Feng, J. McCaffrey and S. Charbonneau, Optical studies of III-V Self-assembled semiconductor quantum dots, Physics in Canada, Sept./Oct. 267 (1996).

[33] A. Wojs, P. Hawrylak, S. Fafard, L. Jacak. Electronic structure and magneto-optics of self-assembled quantum dots, Phys. Rev. B **54**, 5604 (1996).

[34] S. Fafard, Z. Wasilewski, J. McCaffrey, S. Raymond, and S. Charbonneau, InAs self-assembled quantum dots on InP by molecular beam epitaxy, Appl. Phys. Lett. **68**, 991 (1996).

[35] M. Grundmann, N.N. Ledentsov, O. Stier et al. Excited states in self-organized InAs/GaAs quantum dots: theory and experiments. Appl. Phys. Lett. **68**, 979 (1996).

[36] H. Lipsanen, M. Sopanen, J. Ahopelto. Luminescence from excited states in strain-induced $In_xGa_{1-x}As$ quantum dots. Phys. Rev. B **51**, 13 868 (1995).

[37] S. Fafard, R. Leon, D. Leonard, J.L. Merz and P.M. Petroff, Phonons and radiative recombination in self-assembled quantum dots, Phys. Rev. B **52**, 5752 (1995).

[38] J.H. Davies. "The physics of low-dimensional semiconductors", Cambridge University Press, Cambridge, pp. 22-30 (1997).

[39] C. Weisbuch and B. Vinter. "Quantum Semiconductor Structures", Academic Press, San Diego, Chap.1 (1991).

[40] S. Raymond. Zero-dimensional properties of self-assembled islands. Ph.D. thesis, University of Ottawa (1997).

[41] U. Woggon. "Optical Properties of Semiconductor Quantum Dots", Springer, Berlin Heidelberg, Chap 3 (1997).

[42] S. Fafard, E. Fortin, A.P. Roth. Sequential study of the component layers of a semiconductor quantum-well system. Can. J. Phys. **69**, 346 (1991).

[43] M. Grundmann, O. Stier, D. Bimberg. InGaAs/GaAs pyramidal quantum dots: strain distribution, optical phonons, and electronic structure. Phys. Rev. B **52**, 11969 (1995).

[44] S. Fafard, S. Raymond, G. Wang et *al.* Temperature effects on the radiative recombination in self-assembled quantum dots. Surf. Science **361/362**, 778 (1996).

[45] G. Bacher, H. Schweizer, J. Kovac et *al.* Influence of barrier height on carrier dynamics in strained $In_xGa_{1-x}As$/GaAs quantum wells. Phys. Rev. B **43**, 9312 (1991).

[46] G. Bastard. "Wave mechanics applied to semiconductor heterostructures", Les éditions de la physique, Paris, Chap. VII (1988)

[47] K. Hess, B.A. Vojak, N. Holonyak, Jr., R. Chin. Temperature dependence of threshold current for a quantum-well heterostructure laser. Solid-State Electron. **23**, 585 (1980).

[48] G. Lasher, F. Stern. Spontaneous and stimulated recombination radiation in semiconductors. Phys. Rev. **133**, A553 (1964).

[49] M.J. Adams. Theoretical effects of exponential band tails on the properties of the injection laser. Solid-State Electron. **12**, 661 (1969).

[50] H. Kawanishi in "Handbook of semiconductor lasers and photonic integrated circuits". Y. Suematsu and A.R. Adams eds, Chapman and Hall, London, Chap. 10, p. 334 (1994).

[51] L.V. Asryan and R.A. Suris. Inhomogeneous line broadening and the threshold current density of a semiconductor quantum dot laser, Semicond. Sci. Technol. **11** 554 (1996).

[52] Y. Kokubun in "Handbook of semiconductor lasers and photonic integrated circuits". Y. Suematsu and A.R. Adams eds. Chapman and Hall, London ,Chap. 3 (1994).

[53] H. Kogelnik in "Integrated optics", T. Tamir ed. Springer-Verlag, Berlin, p.53 (1975)..

[54] H. Kogelnik in "Guided-wave optoelecronics". T. Tamir ed., Springer-Verlag, Heidelberg, Second edition, Chap. 2 (1990).

[55] D. Moss, D. Landheer, A. Delage, F. Chatenoud, M. Dion. Laser compatible waveguide electroabsorption modulator with high contrast and low operating voltage in GaAs/AlGaAs. IEEE Photon. Tech. Lett. **3**, 645 (1991).

[56] S. Raymond, S. Fafard, P.J. Poole, A. Wojs, P. Hawrylak, and S. Charbonneau. State filling and time-resolved photoluminescence of excited states in $In_xGa_{1-x}As/GaAs$ self-assembled quantum dots, Phys. Rev. B **54**, 11548 (1996).

[57] D. Leonard, S. Fafard, K. Pond, Y.H. Zhang, J.L. Merz, and P.M. Petroff, Structural and optical properties of self-assembled InGaAs quantum dots, J. Vac. Sci. Technol. B **12**, 2516 (1994).

[58] M. Asada in "Handbook of semiconductor lasers and photonic integrated circuits". Y. Suematsu and A.R. Adams eds. Chapman and Hall, London, Chap. 7 (1994).

[59] S. Fafard et al, *unpublished.*

[60] J.M. Garcia, G. Medeiros-Ribeiro, K. Schmidt, T. Ngo, J.L. Feng, A. Lorke, J. Kotthaus, P.M. Petroff. Intermixing and shape changes during the formation of InAs self-assembled quantum dots. Appl. Phys. Lett. **71**, 2014 (1997).

[61] G.J. Davies, T. Kerr, C.G. Tuppen, B. Wakefield, and D.A. Andrews. The growth and characterization of nominally undoped $Al_{1-x}In_xAs$ grown by molecular beam epitaxy, J. Vac. Sci. Technol. **B 2**, 219-223 (1984).

[62] Z.R. Wasilewski, M.M. Dion, D.J. Lockwood, P. Poole, R.W. Streater and A.J. SpringThorpe. Composition of AlGaAs, J. Appl. Phys. **81**, 1683 (1997).

[63] Landolt-Börnstein, "Numerical data and functional relationships in science and technology", volume 22a Springer-Verlag, Berlin (1987).

[64] S.H. Pan, H. Shen, Z. Hang, F.H. Pollack, W. Zhuang, Q. Xu, A.P. Roth, R.A. Masut, C. Lacelle, D. Morris. Photoreflectance study of narrow-well strained-layer $In_xGa_{1-x}As/GaAs$ coupled multiple-quantum-well structures, Phys. Rev B **38**, 3375 (1988).

[65] J.Y. Marzin, M.N. Charasse, B. Sermage. Optical investigation of a new type of valence-band configuration in $In_xGa_{1-x}As$-GaAs strained superlattices, Phys. Rev. B **31**, 8298 (1985).

[66] O.J. Glembocki, K. Takarabe in "Handbook of optical constants of solids II". E.D. Palik ed. Academic Press, Boston, p. 513 (1991).

[67] R. Leon, P.M. Petroff, D. Leonard, S. Fafard. Spatially resolved visible luminescence of self-assembled semiconductor quantum dots Science, **267**, 1966 (1995).

[68] R. Leon, S. Fafard, D. Leonard, J.L. Merz, P.M. Petroff. Visible luminescence from semiconductor quantum dots in large ensembles, Appl. Phys. Lett. **67**, 521 (1995).

[69] Q. Xie, A. Madhukar, P. Chen, and N.P. Kobayashi. Vertically self-organized InAs quantum box islands on GaAs(100), Phys. Rev. Lett. **75**, 2542 (1995).

[70] G.S. Solomon, J.A. Trezza, A.F. Marshall, J.S. Harris, Jr. Vertically aligned and electronically coupled growth induced InAs islands in GaAs, Phys. Rev Lett. **76**, 952 (1996).

[71] S. Raymond, S. Fafard et al. *To be published.*

[72] H. Shoji, K. Mukai, N. Ohtsuka, M. Sugawara, T. Uchida, and H. Ishikawa. Lasing at three-dimensionally quantum-confined sublevel of self-organized $In_{0.5}Ga_{0.5}As$ quantum dots by current injection, IEEE Photonics Technol. Lett. **7**, 1385 (1995).

[73] D. Leonard, K. Pond, P.M. Petroff. Critical layer thickness for self-assembled InAs islands on GaAs. Phys. Rev. B **50**, 11687 (1994).

[74] R. Heitz, M. Grundmann, N.N. Ledentsov et *al*. Multiphonon-relaxation processes in self-organized InAs/GaAs quantum dots. Appl. Phys. Lett. **68**, 361 (1996).

[75] B.R. Bennett, B.V. Shanabrook, R. Magno. Phonons in self-assembled (In,Ga,Al)Sb quantum dots. Appl. Phys. Lett. **68**, 958 (1996).

[76] N. Kirstaedter, N.N. Ledentsov, M. Grundmann, D. Bimberg, V.M. Ustinov, S.S. Ruvinov at al. Low threshold, large T_0 injection laser emission from (InGa)As quantum dots, Electronics Lett. **30**, 1416 (1994).

[77] K. Kamath, P. Bhattacharya, T. Sosnowski, T. Norris, and J. Phillips, Room-temperature operation on $In_{0.48}Ga_{0.52}As$/GaAs self-organised quantum dot lasers, Electronics Lett. **32**, 1374 (1996).

[78] R. Mirin, A. Gossard and J. Bowers, Room temperature lasing from InGaAs quantum dots, Electronics Lett. **32**, 1732 (1996).

[79] H. Saito, K. Nishi, I. Ogura, S. Sogou, and Y. Sugimoto, Room-temperature lasing operation of a quantum-dot vertical-cavity surface-emitting laser, Appl. Phys. Lett. **69**, 3140 (1996).

[80] Q. Xie, A.Kalburge, P. Chen, and A. Madhukar, Observation of lasing from vertically self-organized InAs three dimensional island quantum boxes on GaAs (001), IEEE Photon. Technol. Lett. **8**, 965 (1996).

[81] Zh.I.Alferov, N.A. Bert, A.Yu. Egorov, A.E. Zhukov, P.S. Kop'ev, A.O. Kosogov et al. An injection heterojunction laser based on arrays of vertically coupled InAs quantum dots in a GaAs matrix, Semiconductors, **30**, 194 (1996).

[82] D.L. Huffaker, L.A. Graham, and D.G. Deppe. Low-threshold continuous-wave operation of an oxide-confined vertical cavity surface emitting laser based on a quantum dot active region and half-wave cavity, Electron. Lett. **33**, 1225 (1997).

[83] E. Kappon, D.M. Hwang, M. Walther, R. Bhat, N.G. Stoffel. Two-dimensional quantum confinement in multiple quantum wire lasers grown by OMCVD on V-grooved substrates, Surf. Sci. **267**, 593 (1992).

[84] H. Shoji, Y. Nakata, K. Mukai, Y. Sugiyama, M. Sugawara, N. Yokoyama, H. Ishikawa. Room temperature CW operation at the ground state of self-formed quantum dot lasers with multi-stacked dot layer, Electon. Lett. **32**, 2023 (1996).

[85] S.Fafard, Z. Wasilewski et al. *To be published.*

IMAGE EVALUATION TEST TARGET (QA-3)

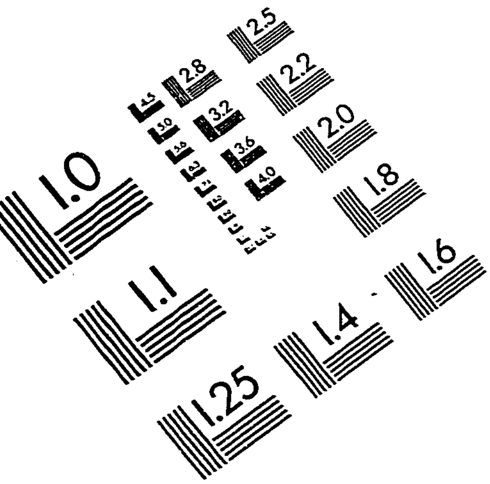

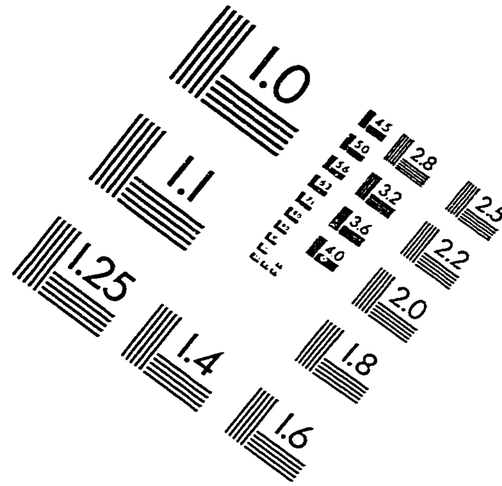

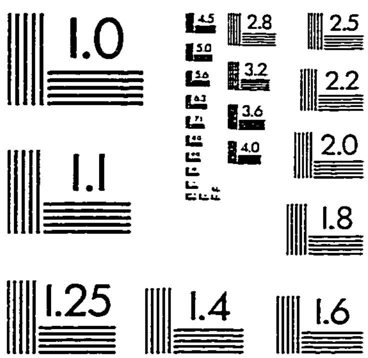

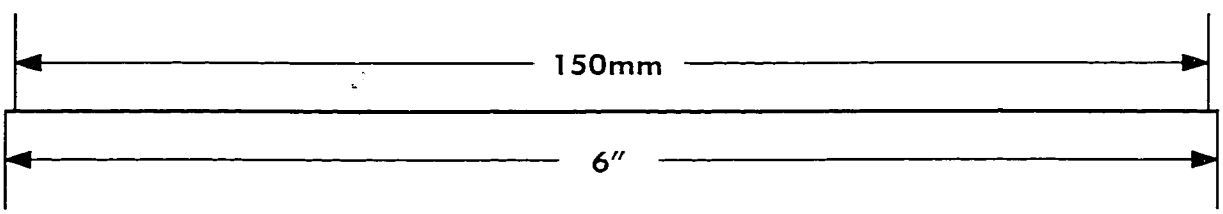

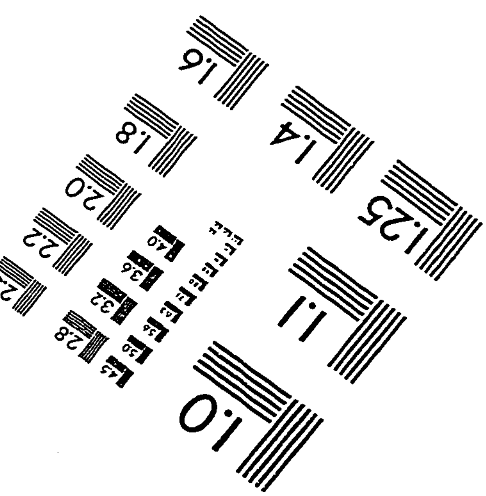

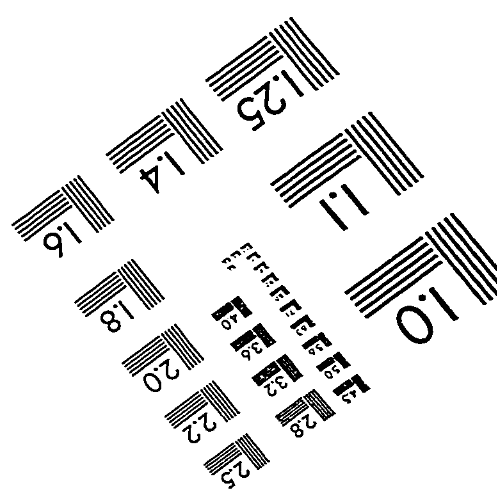

APPLIED IMAGE . Inc
1653 East Main Street
Rochester, NY 14609 USA
Phone: 716/482-0300
Fax: 716/288-5989